The Astrophysical Journal Supplement Series, 198:11 (18pp), 2012 February doi:10.1088/0067-0049/198/2/11

INTERSTELLAR GAS FLOW PARAMETERS DERIVED FROM INTERSTELLAR BOUNDARY EXPLORER-Lo OBSERVATIONS IN 2009 AND 2010: ANALYTICAL ANALYSIS

E. Möbius[1], P. Bochsler[1], M. Bzowski[2], D. Heirtzler[1], M. A. Kubiak[2], H. Kucharek[1], M. A. Lee[1], T. Leonard[1], N. A. Schwadron[1], X. Wu[1], S. A. Fuselier[3], G. Crew[4], D. J. McComas[5,6], L. Petersen[1], L. Saul[7], D. Valovcin[1], R. Vanderspek[4], and P. Wurz[1]

[1] Space Science Center and Department of Physics, University of New Hampshire, Durham, NH 03824, USA
[2] Space Research Centre, Polish Academy of Sciences, Warsaw, Poland
[3] Lockheed Martin Advanced Technology Laboratory, Palo Alto, CA, USA
[4] Massachusetts Institute of Technology, Cambridge, MA, USA
[5] Southwest Research Institute, San Antonio, TX, USA
[6] Department of Physics and Astronomy, University of Texas, San Antonio, TX, USA
[7] Physikalisches Institut, Universität Bern, Bern, Switzerland
Received 2011 August 1; accepted 2011 October 12; published 2012 January 31

ABSTRACT

Neutral atom imaging of the interstellar gas flow in the inner heliosphere provides the most detailed information on physical conditions of the surrounding interstellar medium (ISM) and its interaction with the heliosphere. The *Interstellar Boundary Explorer* (*IBEX*) measured neutral H, He, O, and Ne for three years. We compare the He and combined O + Ne flow distributions for two interstellar flow passages in 2009 and 2010 with an analytical calculation, which is simplified because the *IBEX* orientation provides observations at almost exactly the perihelion of the gas trajectories. This method allows separate determination of the key ISM parameters: inflow speed, longitude, and latitude, as well as temperature. A combined optimization, as in complementary approaches, is thus not necessary. Based on the observed peak position and width in longitude and latitude, inflow speed, latitude, and temperature are found as a function of inflow longitude. The latter is then constrained by the variation of the observed flow latitude as a function of observer longitude and by the ratio of the widths of the distribution in longitude and latitude. Identical results are found for 2009 and 2010: an He flow vector somewhat outside previous determinations ($\lambda_{\mathrm{ISM}\infty} = 79.^{\circ}0 + 3.^{\circ}0(-3.^{\circ}5)$, $\beta_{\mathrm{ISM}\infty} = -4.^{\circ}9 \pm 0.^{\circ}2$, $V_{\mathrm{ISM}\infty} = 23.5 + 3.0(-2.0)$ km s^{-1}, $T_{\mathrm{He}} =$ 5000–8200 K), suggesting a larger inflow longitude and lower speed. The O + Ne temperature range, $T_{\mathrm{O+Ne}} =$ 5300–9000 K, is found to be close to the upper range for He and consistent with an isothermal medium for all species within current uncertainties.

Key words: ISM: atoms – ISM: clouds – ISM: kinematics and dynamics – methods: data analysis – solar neighborhood – Sun: heliosphere

Online-only material: color figures

1. INTRODUCTION

The local Galactic environment of the Sun consists of a warm, relatively dilute, partially ionized, and quite structured interstellar gas cloud (e.g., reviews by Cox & Reynolds 1987; Frisch 1995). The Sun appears to be close to a cloud boundary, possibly with a significant gradient in the ionization fraction of He (e.g., Cheng & Bruhweiler 1990; Wolff et al. 1999; Slavin & Frisch 2002). The environment and structure of the local interstellar cloud (LIC), including its integral densities and relative speeds, have been studied on scales of several parsecs through UV line absorption by the surrounding medium in the light of nearby stars (e.g., McClintock et al. 1978; Frisch 1981; Crutcher 1982; Lallement & Bertin 1992; Linsky et al. 1993). In a recent workshop "From the Heliosphere to the Local Bubble" at the International Space Science Institute in Bern, Switzerland, the heliosphere and its surroundings were discussed in the context of their more extended environment of the Local Bubble (Möbius 2009, and references therein), while Frisch et al. (2009) provided an overview of the solar neighborhood in the context of the Interstellar Boundary Explorer (*IBEX*) objectives. The influence of the interstellar gas reaches deep into the heliosphere, for example, with the generation of pickup ions (e.g., Möbius et al. 1985; Gloeckler & Geiss 1998) and of anomalous cosmic rays (e.g., Klecker 1995; Jokipii 1998) as well as a slowdown of the solar wind, especially when approaching the termination shock (Richardson et al. 1995).

Conditions in the surrounding interstellar medium (ISM) have changed dramatically over the history of the solar system (for a recent comprehensive compilation see Frisch 2006), with important consequences for the heliosphere. In particular, the inventory of neutral interstellar gas, its spatial distribution, and its products in the inner heliosphere change substantially with external conditions, as does their filtering at the interface, which changes the abundances of the interstellar neutrals that enter the heliosphere through species-specific charge exchange in the heliospheric boundary layers (Möbius et al. 2006; Müller & Zank 2004; Zank et al. 2006). The heliosphere is moving through a succession of warm clouds within the hot and very dilute plasma of the Local Bubble that are similar to the one it is currently in and, in fact, may be in transition to another cloud (Redfield 2008).

Neutral ISM gas flows through the inner heliosphere and thus can be used for diagnostics of the surrounding medium with a variety of space-borne remote sensing and in situ methods. While approaching the Sun, the interstellar wind of many neutral species is depleted by ionization to various degrees and deflected by the Sun's gravitational field (modified by radiation pressure for H), thus forming a characteristic flow pattern and density structure with a cavity close to the Sun and gravitational focusing

on the downwind side (for all species except H, which forms a shadow; McComas et al. 2004). For early reviews on this topic, see, e.g., Axford (1972), Fahr (1974), and Holzer (1977).

Some interstellar constituents (e.g., He and Ne) flow through the heliospheric boundary mostly unimpeded. For others (notably H and O) a substantial fraction interacts with the plasma in the outer heliosheath by charge exchange. In turn, a population from the heliosheath appears in the heliosphere as a secondary neutral component via the same charge exchange, thus providing the opportunity to diagnose physical processes in the outer heliosheath beyond the heliopause. To understand these interactions and to make sense of observations of the resulting particle populations requires detailed global modeling of the heliosphere, which has made substantial advances over the past 10 years. For recent overviews of the various modeling methods and their comparison, see, e.g., Fahr et al. (2000), Zank & Müller (2003), Alexashov & Izmodenov (2005), Müller et al. (2008), and Zank et al. (2009).

Local inferences about the interstellar gas distribution in the inner heliosphere were first made with UV backscatter observations of H (e.g., Bertaux & Blamont 1971) and He (e.g., Weller & Meier 1974). More recently, pickup ion measurements of He (Möbius et al. 1985) and H (Gloeckler et al. 1992) provided a complementary in situ technique for these species, which also provides access to minor species (Gloeckler & Geiss 2001). Finally, direct neutral gas flow observations (Witte et al. 1996) supply the most detailed information about the kinetic parameters of the ISM flow but so far have been the most challenging and only available for He. A preliminary consolidation of the results with a combination of these local observation methods for He presented in meetings of the science team "Physical Parameters of the Local Interstellar Medium (LISM) through Coordinated Observations of the Gravitational Focusing Cone at 1 AU" at the International Space Science Institute (ISSI) led to a set of consensus values for the ISM He parameters (Möbius et al. 2004). Möbius et al. (2004) also give a detailed account of the previous state of ISM neutral diagnostics in the inner heliosphere.

With its unprecedented capability to image neutral atom distributions, the *IBEX* (McComas et al. 2009a, 2009b; see also other references in the *IBEX* special issue of Space Science Reviews) is now providing a new look at the interstellar gas flow through the inner heliosphere (Möbius et al. 2009b). In its first 6 month series of energetic neutral atom (ENA) maps, the IBEX-Lo sensor (Fuselier et al. 2009) observed the interstellar He flow distribution with unprecedented counting statistics at Earth's orbit and measured directly the neutral ISM O and H flow for the first time (Möbius et al. 2009a). It was noted in this initial paper that the observed locations of the flow distribution in the sky are roughly consistent with the previous interstellar He parameters and that the O distribution is consistent with a similar temperature for O and He. Furthermore, indications for a secondary component of O and perhaps of He were found (Möbius et al. 2009a).

In this paper, we present a detailed analysis of the He ISM flow as observed in 2009 and 2010. We reevaluate the interstellar He flow parameters in light of the new *IBEX* observations. We also compare our observations with an analytical model of the interstellar gas flow by making use of the specific observation strategy with *IBEX*, which captures the interstellar flow trajectories almost exactly at their perihelion at 1 AU and thus greatly simplifies analytical treatment of the observations, as discussed in detail in the paper by Lee et al. (2012). In a companion paper, Bzowski et al. (2012) compare the *IBEX* He flow observations with their test particle model, based on a hot model of the ISM (e.g., Tarnopolski & Bzowski 2008) taking into account spatial and temporal variations of all relevant ionization rates. In addition, Bochsler et al. (2012) present an analysis of interstellar heavy neutral atom flow, which had previously been expected to represent mainly ISM O (Möbius et al. 2009b). However, they find that it contains a mixture of interstellar O and Ne of similar proportions at 1 AU and present a method to deduce an approximate Ne abundance in the LIC. Here, we use the Bochsler et al. (2012) results as input to determine the O and Ne temperatures. Finally, Saul et al. (2012) examine the ISM H observations.

In this paper, we start in Section 2 with a brief review of the instrumentation, *IBEX* observation strategy, and data selection. We then follow a path of increasing sophistication in the analysis, starting in Section 3 with a determination of a relation between the ISM flow speed and direction in ecliptic longitude outside the heliosphere from the location of the flow maximum. In Section 4, the peak location and width in ecliptic latitude for He and the O + Ne mixture at the maximum flow location are used to deduce the inflow latitude and temperature outside the heliosphere as a function of inflow longitude according to the relation found in Section 3. In Section 5, we use the dependence of the observed peak latitude at 1 AU as a function of observer longitude and the ratio of the width in longitude and latitude to place constraints on the inflow longitude outside the heliosphere and present an updated set of interstellar flow parameters, which are then discussed in Section 6.

2. INSTRUMENTATION, OBSERVATION STRATEGY, AND DATA SELECTION

2.1. Overview of the IBEX Mission

The *IBEX* spacecraft was launched into a highly elliptical Earth orbit with an apogee of ≈50 R_E in 2008 October. It was designed to observe heliospheric and interstellar ENAs with as little interference from terrestrial and magnetospheric background as possible. *IBEX*, a small explorer mission (McComas et al. 2009a), carries two single-pixel high-sensitivity ENA cameras, IBEX-Hi (Funsten et al. 2009) and IBEX-Lo (Fuselier et al. 2009), whose fields of view (FoV) point radially outward into two opposite directions and whose combined energy range is 10–6000 eV with overlap between 300 and 2000 eV. *IBEX* is a roughly Sun-pointing, spinning satellite, whose spin axis is re-oriented toward the Sun after completion of each 7–8 day orbit so that complete full-sky ENA maps are obtained with a resolution of the 7° FWHM FoV of the sensors over a period of 6 months. As a consequence, *IBEX* samples the heliospheric and interstellar ENA distributions at 1 AU in a plane that is approximately perpendicular to the Earth–Sun line. This is equivalent to observing ENAs that arrive from the heliospheric boundary or beyond at the perihelia of their trajectories, independent of their flow direction at infinity. This measurement geometry simplifies the analysis of the interstellar neutral gas flow, as described in detail in the paper by Lee et al. (2012).

2.2 IBEX-Lo Sensor

The IBEX-Lo sensor was optimized for the observation of the interstellar neutral gas flow of several species, while at the same time measuring ENAs in the energy range 10–2000 eV from the heliospheric boundary (Fuselier et al. 2009). IBEX-Lo makes use of a large-area collimator to define the 7° FWHM

FoV. Successive negatively biased rejection rings and a positive potential at the collimator repel electrons and ions, allowing only neutral atoms and photons to enter the sensor. While the electron rejection works as designed, the positive potential cannot be applied to the collimator. However, the internal potential configuration of IBEX-Lo still prevents all ions with energies <200 eV from reaching the conversion surface, with partial rejection capability between 200 and 1000 eV. ENAs (and ions >200 eV) that pass the collimator reach the conversion surface, where a small fraction is converted to negative ions. These negative ions are selected for energy/charge within eight logarithmically spaced energy steps by an electrostatic analyzer, which also rejects any neutrals and positive ions. Serrations and blackening of the analyzer deflection surfaces also efficiently suppress photons. After a +16 kV post-acceleration, negative ions are analyzed for their mass in a two-section time-of-flight (TOF) spectrometer. Triple coincidence conditions very effectively reject nearly all background. The central electronics unit (CEU) sorts the resulting pulse height events based on their coincidence condition (giving triple coincidence events the highest priority) and inserts a time tag, counting time from each spin pulse. All events identified as H and O by the TOF spectrometer are sorted into angle histograms with 6° bins according to their energy steps. IBEX-Lo is described in detail by Fuselier et al. (2009).

The triple coincidence TOF spectrometer of IBEX-Lo determines the mass of incoming neutral atoms directly for those species (e.g., H and O) that are turned into negative ions at the conversion surface. However, noble gases, such as He and Ne, that do not produce enough negative ions for detection or none at all (Smirnov 1982) still generate sputtered negative ions (H, C, and O) from the conversion surface. These negative ions are detected and identified by the IBEX-Lo TOF spectrometer (Wurz et al. 2008; Möbius et al. 2009b). Since the IBEX-Lo sensor was also calibrated for its response to He and Ne at a variety of energies (Fuselier et al. 2009; Möbius et al. 2009b), the observed ratios of H, C, and O are used to infer the identity (He or Ne) of the incoming noble gas atoms. Figure 1 shows schematically the response of the IBEX-Lo conversion surface to an incoming mono-energetic ENA beam for the two different groups of species, along with the energy response of the electrostatic analyzer. An H or O beam produces a negative ion distribution (red dashed curve in the lower panel of Figure 1) that is shifted slightly to lower energy and contains a low-energy tail, thus allowing determination of the incoming energy at roughly the resolution of the electrostatic analyzer. In contrast, He and Ne generate a broad energy distribution of sputtered ions that starts below the incoming energy and extends down to very low energies (blue dashed curve in the lower panel of Figure 1). From the upper energy cutoff of this observed sputtered ion distribution, one can determine only whether the incoming neutral flow at 1 AU consists of He or Ne. The original energy of the neutral He or Ne cannot be determined. To deduce quantitatively the inflow speed of interstellar gas outside the heliosphere from these observations, one has to determine the Keplerian trajectory of the gas flow from infinity to 1 AU (Lee et al. 2012). This requires knowledge of the direction of the incoming neutral atoms at the point of observation and thus the exact pointing of IBEX-Lo.

The precise pointing direction of IBEX-Lo relative to accurately known star positions is determined independently of any mechanical and thermal tolerances of the spacecraft, using a star sensor contained in IBEX-Lo whose boresight is co-aligned with that of the IBEX-Lo collimator to better than 0.°1 (Fuselier et al. 2009). We have verified that the pointing determination with both the star sensor and star tracker indeed agrees to within 0.°1 for time periods when identifiable stars are in the star sensor's FoV and the *IBEX* star tracker has been operating within specifications, as discussed by Hlond et al. (2012). Therefore, sensor pointing can be taken from the spacecraft attitude information for the time periods when the *IBEX* star tracker is not affected by bright Earth and Moon signals.

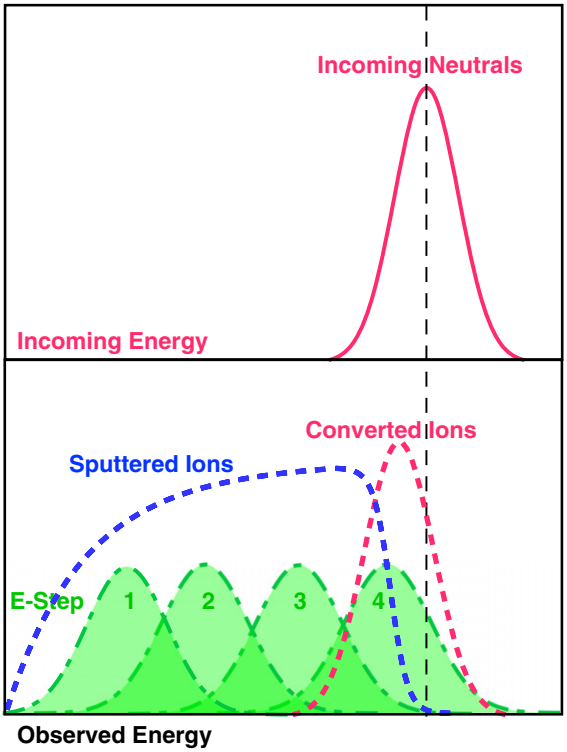

Figure 1. Schematic representation of method used to determine the identity and energy of an incoming neutral atom. Upper panel: energy selection of an incoming mono-energetic neutral atom beam (full red curve) by the electrostatic analyzer of IBEX-Lo. Lower panel: negative ions from conversion of incoming neutrals of the same species (i.e., from H and O) have energies represented by the red dashed curve. Sputtered negative ions (H, C, and O) generated at the conversion surface from He and Ne produce an energy distribution shown by the blue dashed curve. While the ≈50% wide electrostatic analyzer energy acceptance bands (green dash-dotted curves) allow only a rough energy analysis of converted negative ions, sputtered ions are detected in all energy bands below the energy of the incoming neutral atoms. The shapes of the dashed blue curve are different for He and Ne, allowing identification of the incoming neutrals.

2.3. Observational Strategy for the Interstellar Flow

A schematic view of the interstellar He gas distribution in the inner heliosphere is shown in Figure 2 along with typical trajectories of the bulk flow. The interstellar neutral gas flow is observed tangentially to Earth's orbit and thus at the perihelion of the incoming gas trajectories because the *IBEX* spin axis points toward the Sun and the sensor FoVs point perpendicular with respect to the spin axis and radially outward. The observation at perihelion of the ISM flow trajectories is limited to a location and time in each orbit when the spin axis points exactly along the Earth–Sun line in the ecliptic plane. After re-orientation of the *IBEX* spin axis to ≈1° east of the Sun shortly after perigee, which is the current *IBEX* operational strategy, the actual orientation drifts at a rate of slightly less than $1^\circ\ \mathrm{day}^{-1}$ westward over the course of the orbit. It should be noted

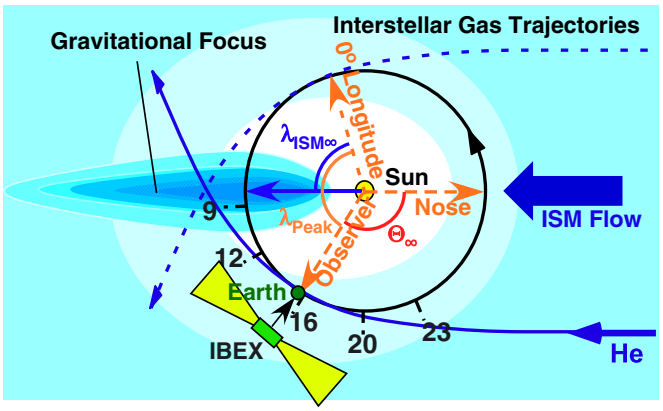

Figure 2. Schematic view of the interstellar gas flow distribution for He in the inner heliosphere along with ISM bulk flow trajectories that are observable with *IBEX* at 1 AU. The ISM flow direction at infinity, $\lambda_{ISM\infty}$, and the observer location to detect the flow maximum at 1 AU, λ_{Peak}, are shown relative to the spring equinox (0° longitude). θ_∞ is the angle swept out by the ISM bulk flow trajectory from infinity to the observer or the true anomaly at infinity.

that the *IBEX* spin axis always points toward slightly positive latitude (≈0.°7–1°). Here, we evaluate ISM flow observations at perihelion and thus for almost exact Sun-pointing of the spin axis in the ecliptic plane. The observer location will be referred to as "Sun-pointing location" in the rest of this paper.

For now, we adopt the ISM flow speed, $V_{ISM\infty}$, to be 26.4 km s^{-1}, as derived by Witte (2004), resulting in V_{ISM}(1 AU) of 49.9 km s^{-1} in the rest frame at 1 AU. The prime season for *IBEX* observations is winter to early spring, when the Earth moves into the peak ISM flow at 1 AU (solid blue trajectory curve in Figure 2). The ISM flow speed in the observer frame, V_{ISM}' (1 AU), is then 79.8 km s^{-1}. As a general convention in this paper, we use unprimed symbols (e.g., V_{ISM}) for quantities in the rest frame and primed symbols (e.g. V_{ISM}') for quantities in the observer frame. In spring, the energy of the interstellar He atoms is 132 eV, thus providing high detection efficiency. So far, attempts to obtain a complementary measurement of the flow direction in the fall (dashed blue trajectory curve in Figure 2), when the Earth recedes from the flow and thus the energy for He in the observer frame is only 8 eV, have not been successful. Expected signals have not exceeded ENA flux levels from local sources (i.e., background for this analysis).

Figure 2 also shows the ISM flow direction at infinity $\lambda_{ISM\infty}$ and the observer location for the observation of the maximum ISM flow λ_{Peak} relative to 0° ecliptic longitude (location of the Sun at spring equinox). The angle θ_∞ (true anomaly at infinity) swept out by the interstellar bulk flow trajectory from infinity to its perihelion at 1 AU is related to the observer location and the ISM flow direction as follows:

$$\theta_\infty = \lambda_{ISM\infty} + 180^\circ - \lambda_{Peak}. \quad (1)$$

For the hyperbolic trajectory of the incoming interstellar bulk flow in the Sun's gravitational field, the angle θ_∞ swept out by the radius vector of the trajectory from infinity to perihelion at 1 AU is related to the bulk speed at infinity $V_{ISM\infty}$ by

$$-\frac{1}{\cos(\theta_\infty)} = 1 + \left(\frac{r_E V_{ISM\infty}^2}{GM_s}\right) \quad \text{or}$$

$$V_{ISM\infty} = \sqrt{\frac{GM_s}{r_E} \cdot \left(\frac{-1}{\cos(\theta_\infty)} - 1\right)}, \quad (2)$$

where r_E is the distance from the Sun to the Earth and M_s is the Sun's mass. Equation (2) establishes a fixed relation between $V_{ISM\infty}$ and θ_∞ (and by inference through Equation (1) between $V_{ISM\infty}$ and $\lambda_{ISM\infty}$) that hinges solely on celestial mechanics, where a smaller angle θ_∞ (or $\lambda_{ISM\infty}$) is equivalent to a higher speed $V_{ISM\infty}$ at infinity and vice versa. It should be noted that Equations (1) and (2) also apply to any interstellar neutral atom in the velocity distribution at infinity. Then, we use more generally V_∞, λ_∞ instead of $V_{ISM\infty}$, $\lambda_{ISM\infty}$, as well as λ_{Obs} instead of λ_{Peak}, in these equations.

Figure 3 shows IBEX-Lo maps in a logarithmically spaced color coding scheme taken in 2010 of the observed H count rates produced (a) by sputtering of ISM He and conversion of ISM H at 15 eV (top panel), (b) by sputtering of ISM He at 110 eV (center panel), and (c) for O by conversion of O and sputtering of Ne at 600 eV (bottom panel). The flow peaks can be seen near −130° in ecliptic longitude and coming from a few degrees positive latitude (looking into the flow in these maps). We obtain the ISM flow peak location λ_{Peak} from the distribution in longitude to relate it to $V_{ISM\infty}$ using Equations (1) and (2).

As described in more detail below, we take a key set of angular distributions in latitude at the location where the interstellar flow maximum is observed (indicated by a white line for orbit 64 in the respective maps). In this way, we can use Equation (2) to relate $V_{ISM\infty}$ to $\lambda_{ISM\infty}$ in our deduction of (a) the inflow direction in latitude of the interstellar gas at infinity $\beta_{ISM\infty}$ (from the angle ψ_{Peak}' of the peak in latitude in the observed distribution) and (b) the flow Mach number at infinity $M_{ISM\infty}$ and thus the temperature (T_{He} and T_{O+Ne}) of the interstellar gas (from the observed width σ_ψ', i.e., the standard deviation when adopting a Gaussian velocity distribution; cf. Lee et al. 2012).

As shown in Lee et al. (2012), the ISM flow direction in latitude in the rest frame at 1 AU ψ_{Peak} is geometrically related to the inflow direction in latitude at infinity $\beta_{ISM\infty}$ through

$$\tan\psi_{Peak} = \frac{\tan\beta_{ISM\infty}}{|\sin\theta_\infty|}. \quad (3)$$

The peak directions in the rest frame and in the observer frame are related as follows:

$$\frac{\sin\psi_{Peak}'}{V_{ISM}(1\text{ AU})} = \frac{\sin(\psi_{Peak} - \psi_{Peak}')}{V_E}. \quad (4)$$

Because V_{ISM}(1 AU) depends on $V_{ISM\infty}$ and thus is related to $\lambda_{ISM\infty}$ via Equations (1) and (2), an observation of the location ψ_{Peak}' of maximum ISM flow yields a relation $\beta_{ISM\infty}(\lambda_{ISM\infty})$. Similarly, the observation of the width σ_ψ' of the angular distribution in latitude in the observer frame can be translated into a relation for the flow Mach number at infinity $M_{ISM\infty}(\lambda_{ISM\infty})$. With $M_{ISM\infty} = V_{ISM\infty}/C_\infty$ (C_∞ is the sound speed), this relation leads to $T(\lambda_{ISM\infty})$.

In the following, we deduce the interstellar flow parameters for He ($V_{ISM\infty}$, $\lambda_{ISM\infty}$, $\beta_{ISM\infty}$, and T), starting with a relationship between $V_{ISM\infty}$ and $\lambda_{ISM\infty}$ from Equation (2), which emerges from the location of the observed ISM flow maximum in ecliptic longitude at 1 AU as described above. This strategy allows us to derive these parameters separately, or at least in pairs, rather than finding an optimum solution for the full set of parameters simultaneously as is done in the complementary approach described by Bzowski et al. (2012) or as has been used

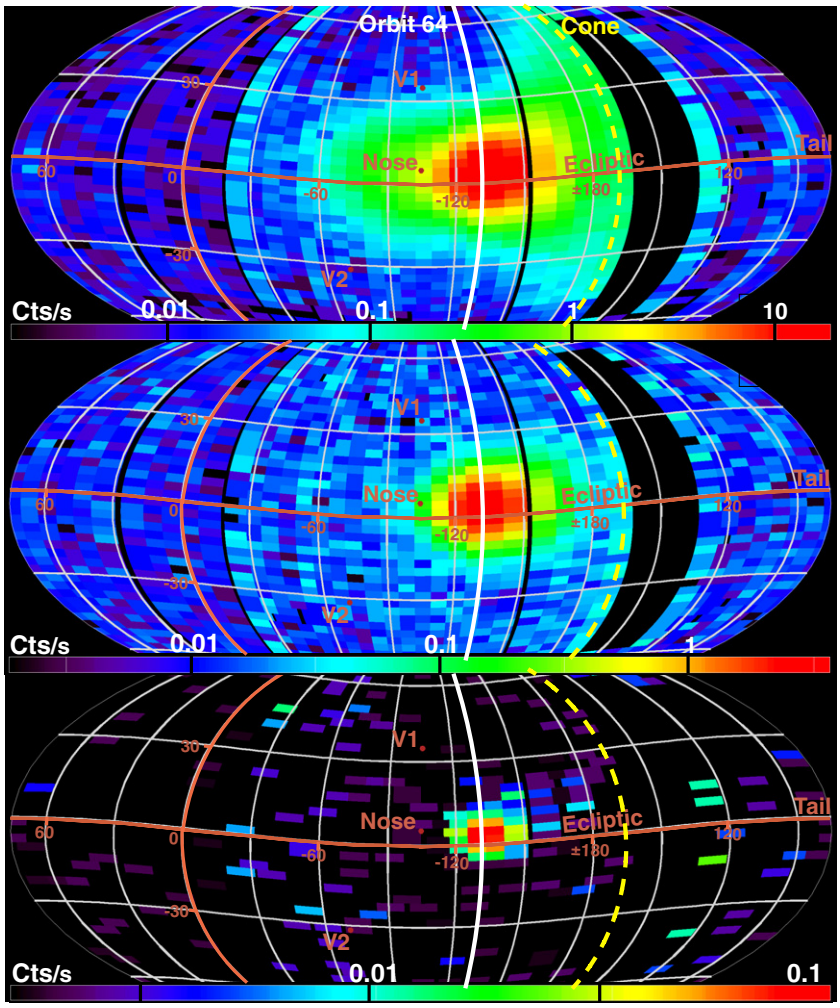

Figure 3. Mollweide projection maps of IBEX-Lo counting rates showing the ISM flow at 1 AU. Shown in the maps are sputtered H due to incoming ISM He and converted ISM H at an incoming energy of ≈15 eV (top panel), sputtered H from He at the maximum energy of He of 110 eV (center panel), and converted O at 600 eV (bottom panel). The He distribution extends from the gravitational focusing cone almost to the nose, H (top panel) appears to arrive from the nose direction, and O shows a much narrower distribution.

by Witte (2004) and Banaszkiewicz et al. (1996). Here, we take a path of increasing sophistication, with first deriving a set of parameters as functions of $\lambda_{\mathrm{ISM}\infty}$ that have a rather small uncertainty around this function, but allow a large range in $\lambda_{\mathrm{ISM}\infty}$. Similarly, we also derive a temperature for the mixture of O and Ne gas. Then, we constrain the results to a narrower range in $\lambda_{\mathrm{ISM}\infty}$ by making use of the variation of the observed ψ'_{Peak} as a function of observer longitude, which is sensitive to the combination of $V_{\mathrm{ISM}\infty}$ and $\lambda_{\mathrm{ISM}\infty}$.

Equations (1)–(4) and the process described above are valid only for the ISM flow at perihelion. However, as described above, the orientation of the spin axis relative to the Sun drifts over the course of each orbit at a rate close to 1° day^{-1} because the spin axis remains fixed in inertial space. To account for this known spin-axis drift, we could either adjust the analytical calculation for the deviation from the ideal pointing through linear corrections (Lee et al. 2012) or fit the variation of the observables (count rate of the flow, peak location, and width of the distribution in latitude) over the course of the orbit with an appropriate function and interpolate (or extrapolate as necessary) to the "Sun-pointing location" as defined above. In the analysis presented here, we use the latter approach; the test particle analysis by Bzowski et al. (2012) uses the former approach.

2.4. Data Selection

In order to determine accurately the interstellar gas flow vector, the pointing of IBEX-Lo has to be known to ≈0.°1 accuracy for the observations used in this analysis. We have demonstrated that the pointing of the IBEX-Lo star sensor and that of the spacecraft star tracker agree within this prescribed accuracy for time periods of simultaneous good observations (Hlond et al. 2012). Therefore, we use data from time periods when the *IBEX* star tracker, which provides precision pointing information for the routine data processing, was operating within its specifications for all analysis that requires exact pointing knowledge, such as the evaluation of the flow distributions in latitude. However, the determination of the ISM flow maximum in ecliptic longitude only requires the use of the count rates, obtained over $\pm 3\sigma$ of the angular distribution from the latitude peak position, as a function of longitude, so this requirement can be relaxed.

During the analysis, it was found that the data transfer through the CEU that formats the information for the telemetry slows down because of the total traffic across the interface and the computational load event rates that exceed ≈10 counts s^{-1}, as observed during the He ISM flow peak. This slowdown produces a modulation in the high-resolution data according to the accumulation scheme into 6° sectors. Therefore, we

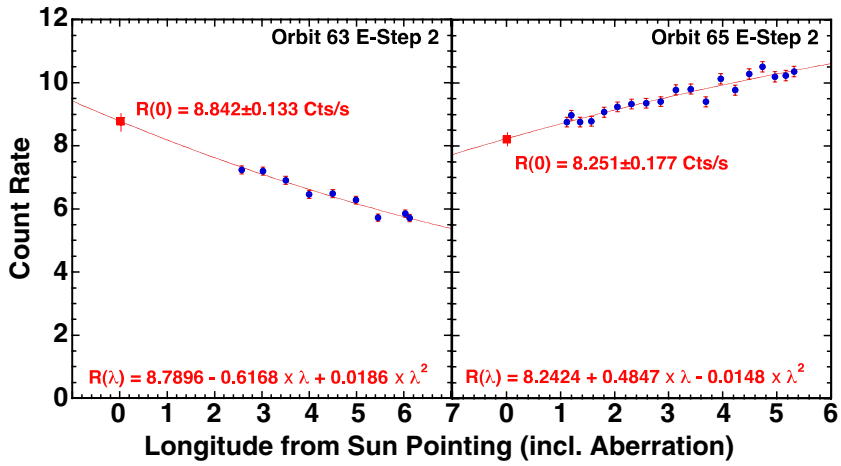

Figure 4. Peak rate as a function of ecliptic longitude for *IBEX* orbits 63 (left panel) and 65 (right panel). The observations are extrapolated to the ecliptic longitude where the ISM flow trajectories are captured at their perihelion, i.e., at the location of exact Sun-pointing of the spin axis corrected for flow aberration due to the spacecraft motion, which is noticeable at the beginning of each orbit. Orbit 63 is usable for the count rate extrapolation but requires too much extrapolation for the peak position determination because of long star tracker blinding.

(A color version of this figure is available in the online journal.)

only use integrated 6° sector data for He in this analysis. In addition, IBEX-Lo detects background electrons, which are easily identified as invalid events by the TOF spectrometer, but they have to be removed by the CEU, which adds to its load and the slowdown when electron rates increase. A more detailed description of these instrumental effects that are taken into consideration can be found in Appendix A.

For this analysis, we have compiled a list of valid time periods for the ISM flow analysis that is used throughout this paper and also in the analysis by Bzowski et al. (2012). Excluded from this list are time periods, for which the following conditions apply:

1. *IBEX* is close to the magnetosphere, where IBEX-Lo observes high count rates of magnetospheric ENAs and ions, based on angular ranges outside the ISM flow distribution.
2. The Moon is in the *IBEX* FoV. These times are taken from the ISOC command files, which contain special commanding for the star sensor.
3. The electron rates for IBEX-Lo are high. These times are identified in the IBEX-Lo TOF count rates, when the otherwise very stable base count rate outside the ISM flow direction is exceeded by more than a factor of 1.6 (safely above any stochastic fluctuations of the base count rate, but low enough to indicate any significant electron rate increases).
4. The star tracker function has been impaired. This affects the determination of the ISM peak location and width in latitude.

No further culling for increased background counts (routinely performed for suprathermal ENA observations; McComas et al. 2009b) is necessary for ISM flow observations because of the concentrated angular distributions at much higher rates. The time periods used for the analysis of the ISM flow are compiled in Table 1 separately for the total count rate and the angular distribution analysis. The angular distribution analysis, in general, is performed on much shorter "good" time periods than the count rate analysis because nominal operation of the star tracker is required. Because the rate analysis requires contiguous time sections of fixed length to achieve approximately comparable counting statistics for each data point, very small portions at the beginning or end of the "good" time intervals may be unused, which accounts for the occasional foreshortening of the "good" time intervals for the rate analysis at the beginning or the end.

3. DETERMINATION OF THE ISM INFLOW SPEED AND LONGITUDE AT INFINITY FROM THE OBSERVED FLOW MAXIMUM AT 1 AU IN ECLIPTIC LONGITUDE

As can be seen from Figure 3, the ISM flow maximum is concentrated in a narrow range of ecliptic longitude. Over the course of approximately three orbits before and after the maximum, the count rate drops by about 1 order of magnitude. Therefore, the evolution of the count rates from orbit to orbit can be used to effectively deduce the location of the maximum as a function of ecliptic longitude of the observer. However, as can be seen in Figure 4, the count rate also varies substantially over the 7–8 days of an orbit. Shown in Figure 4 is the ISM count rate as a function of observer longitude (which is synonymous with time) from the "Sun-pointing location" for orbit 63 (left panel) and orbit 65 (right panel). Generally, the count rate decreases with time during an orbit before reaching the maximum ISM flow (orbit 63) and increases over the orbit after passing the maximum (orbit 65), with almost no variation during the orbit at the flow maximum. In Figure 4, we have determined the count rates of H in energy step 2 (29 eV) integrated over the latitudinal distribution between $\pm 3\sigma$ of the peak over 40 spins, normalized to the 6σ width of the distribution. To extract the true count rate of ISM He, we have subtracted the background from heliospheric ENAs, using a uniform background as obtained in a maximum likelihood fit to the angular ISM flow distribution described in Section 4.1. Figure 4 also shows for each example a least-squares fit line through the data points along with the inter(extra)polated value for the count rate at the ecliptic longitude of the "Sun-pointing location" with the statistical uncertainty for this value.

At the "Sun-pointing location," viewing of the ISM flow at its exact perihelion is only possible if the spacecraft velocity relative to the Earth is very slow. However, because the *IBEX* spin axis is oriented toward the Sun near the beginning of each orbit, i.e., only hours after perigee of the orbit, the key ISM flow observations are made when the spacecraft velocity is between

Table 1
IBEX-Lo ISM Flow Observation Periods

Orbit	SunPt Longitude	Good Times for Rates (year/m:d:h:m:s–m:d:h:m:s)	Good Times for Angular Distributions	Other Conditions
2009				
0012	105.24	2009/01:02:18:23:37–01:02:22:26:04		
		2009/01:03:01:27:10–01:06:19:36:05	2009/01:03:15:28:18–01:06:19:39:58	
		2009/01:06:23:36:34–01:08:18:44:31	2009/01:06:21:29:53–01:07:01:51:34	
			2009/01:07:02:53:37–01:08:03:00:48	
			2009/01:08:04:33:38–01:08:05:50:36	
			2009/01:08:10:28:24–01:08:20:13:20	
0013	109.59	2009/01:10:09:39:30–01:15:03:45:17	2009/01:14:07:25:58–01:14:20:39:06	Not in $\psi'_{\rm Peak}(\lambda_{\rm Obs})$ Long Extrapol.
			2009/01:14:21:40:53–01:15:09:29:07	
0014	117.47	2009/01:18:05:37:40–01:18:21:42:12		Not in $\psi'_{\rm Peak}(\lambda_{\rm Obs})$ Long Extrapol.
		2009/01:20:01:41:16–01:20:17:41:58		
		2009/01:21:04:43:26–01:21:16:45:39		
		2009/01:21:23:43:20–01:23:15:45:07	2009/01:21:22:07:33–01:23:17:44:34	
0015	124.9	2009/01:24:18:44:23–01:25:18:44:26	2009/01:24:16:41:34–01:24:18:44:56	
			2009/01:24:19:31:01–01:25:01:55:02	
			2009/01:25:04:44:00–01:25:19:41:38	
		2009/01:29:20:59:53–01:31:12:29:36	2009/01:29:19:57:05–01:31:06:36:35	
			2009/01:31:09:56:17–01:31:12:45:15	
0016	132.81	2009/02:01:18:22:37–02:03:08:21:38	2009/02:01:17:20:06–02:03:08:18:06	Use Av. $\psi'_{\rm Peak}$, σ'_{ψ}
0017	140.78	2009/02:09:11:57:46–02:14:01:58:06	2009/02:09:05:47:14–02:09:08:46:54	Not in $\psi'_{\rm Peak}(\lambda_{\rm Obs})$ Intervals too short
		2009/02:14:16:32:51–02:15:02:31:45		
		2009/02:15:02:31:45–02:15:19:41:09	2009/02:15:16:32:40–02:15:23:26:39	
0018	148.59	2009/02:17:08:40:02–02:18:20:32:18	2009/02:17:00:38:02–02:18:21:44:25	
		2009/02:19:01:31:59–02:21:21:23:00	2009/02:18:23:50:04–02:20:17:27:04	
		2009/02:22:13:20:26–02:23:17:14:17	2009/02:23:14:23:27–02:23:16:14:16	
0019	156.23	2009/02:24:17:28:44–03:02:13:32:48	2009/02:24:18:20:54–02:27:08:09:05	
			2009/02:27:08:39:41–03:01:14:54:08	
2010				
0060	102.61	2010/01:03:00:24:59–01:05:22:27:09	2010/01:04:12:08:30–01:05:23:44:01	
		2010/01:06:02:25:16–01:09:16:27:23	2010/01:06:01:46:55–01:09:17:05:52	
0061	110.46	2010/01:10:17:47:27–01:11:11:46:03		
		2010/01:11:19:46:06–01:17:07:45:05	2010/01:11:23:13:27–01:17:08:27:08	
0063	125.12	2010/01:26:22:26:52–02:01:16:28:30	2010/01:31:21:34:16–02:01:15:31:48	Not in $\psi'_{\rm Peak}(\lambda_{\rm Obs})$ Long Extrapol.
0064	133.8	2010/02:02:11:35:58–02:09:00:57:57	2010/02:02:11:35:18–02:02:20:55:56	
			2010/02:07:04:38:34–02:07:19:41:53	
			2010/02:08:18:30:09–02:09:01:57:13	
0065	141.57	2010/02:10:04:14:17–02:17:01:18:24	2010/02:10:02:26:10–02:11:01:37:17	
			2010/02:16:14:11:23–02:17:02:24:10	
0066	149.42	2010/02:18:02:46:08–02:20:13:05:09	2010/02:19:00:58:36–02:20:12:02:13	
		2010/02:20:17:04:49–02:24:09:35:11	2010/02:24:16:00:45–02:24:18:37:39	
0067	156.88	2010/02:25:16:52:17–03:04:09:41:59	2010/02:25:14:51:15–02:25:20:12:21	
			2010/02:25:20:43:13–02:28:10:12:03	

2 and 3 km s^{-1}. In addition, the line of apsides points almost at the Sun during the prime ISM observations, as indicated in Figure 5, which shows the *IBEX* orbit for the location where the ISM flow at perihelion arrives exactly perpendicular to the spin axis (right portion of the figure). Here, the spacecraft velocity has a substantial component perpendicular to the incoming ISM flow, thus producing a noticeable aberration. As a result, the appropriate "Sun-pointing location" for this analysis is the location where, after aberration, the ISM flow at perihelion arrives perpendicular to the spin axis and thus enters exactly the center of the FoV (left portion of the figure). This condition is met at an ecliptic longitude that is lower by the aberration angle. Therefore, we repeat the extrapolation procedure as described above for the location where the aberrated flow enters the center of the FoV. This correction shifts the "Sun-pointing location" to lower longitudes by the aberration angle. The fits for orbits 63 and 65 shown in Figure 4 include the aberration for the "Sun-pointing location." To account for potential systematic uncertainties in this procedure, we add quadratically $\pm 0.^{\circ}2$ ($\approx$20% of the aberration angle) to the overall uncertainty in the longitude determination of the ISM flow maximum at the end of this section.

The analysis has been performed for all orbits in 2009 and 2010 when interstellar He flow was observed. Orbits before orbit 13 in 2009 and before orbit 61 in 2010 have been omitted from further analysis in this paper because elevated fluxes that are

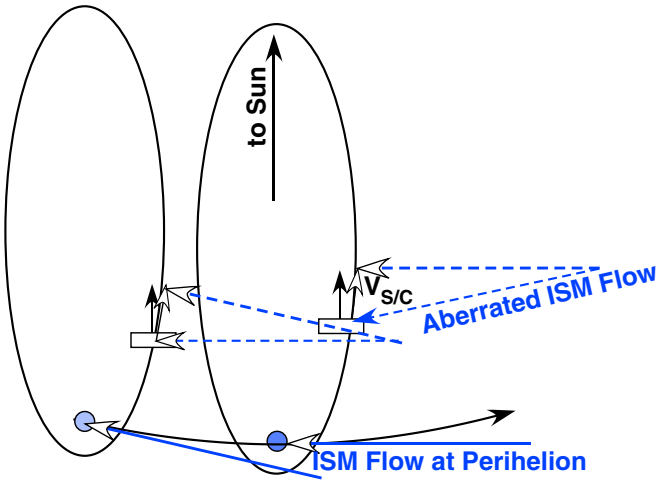

Figure 5. Aberration of the ISM flow at perihelion due to substantial spacecraft motion in the GSE *x*-direction, i.e., perpendicular to the flow, early in each orbit, when the *IBEX* spin axis points exactly at the Sun. The ISM flow at perihelion would in fact be observed as an aberrated flow even earlier as indicated in the left part of the figure.

(A color version of this figure is available in the online journal.)

observed in these orbits even before passage of the gravitational focusing cone of He (yellow dashed line in Figure 3) indicate a secondary component of ISM He (Möbius et al. 2009a; Bzowski et al. 2012). Here, we concentrate on the physical parameters of the pristine ISM.

The analysis of the ISM flow peak in longitude must take into account ionization loss of the observed ISM flux at 1 AU by solar EUV, charge exchange with the solar wind, and electron impact ionization (e.g., McMullin et al. 2004). This reduction in flux increases with the angle, θ_∞, swept out from infinity to the observer at 1 AU. As a consequence, fluxes observed during orbits closer to the focusing cone are systematically more reduced compared to those closer to the ISM inflow direction. This bias leads to an apparent shift of the observed maximum to larger longitudes and can be described as

$$R(\lambda_{\rm Obs}) = R_{\rm o}(\lambda_{\rm Obs}) \cdot e^{-\frac{v_{\rm ISM}(1{\rm AU})}{r_E v_{\rm Ion}}\theta_\infty}, \quad (5)$$

where $R_{\rm o}$ is the expected neutral atom rate without extinction due to ionization on the way in and R is the actually observed rate at $\lambda_{\rm Obs}$, which is related to θ_∞ for each of these locations according to Equation (1). $\nu_{\rm Ion}$ is the total ionization rate for He at 1 AU, averaged over the preceding year. Bzowski et al. (2012) describe how the ionization rates have been obtained.

In addition, it is important to note that IBEX-Lo observes differential fluxes of the ISM flow at 1 AU, while the location of the maximum of the distribution function of the ISM flow marks the actual bulk velocity of the gas. In each orbit, IBEX-Lo samples a different portion of the ISM flow distribution, with slower speeds sampled during earlier orbits (closer to the focusing cone) and faster speeds sampled during later orbits. Rates scale with the observed speeds relative to the phase-space distribution, and thus observed rates are increased according to the faster speeds during later orbits after passing the flow maximum compared with earlier orbits. This bias also leads to an apparent shift of the maximum in the observations to larger longitudes. We correct the observed rates using the difference between differential flux and phase-space density, which scales as $V(1\ {\rm AU})^3$ because, for sputtered ions, the IBEX-Lo sensor

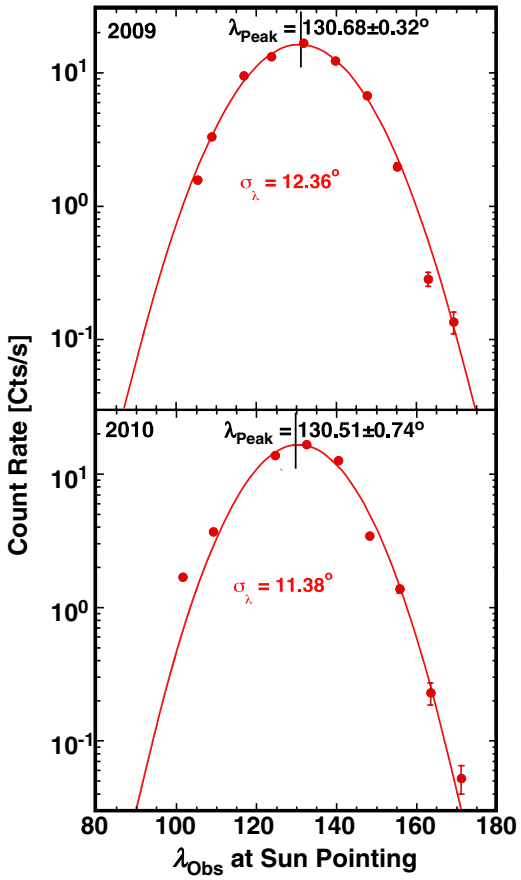

Figure 6. ISM flow rates at exact Sun-pointing for each orbit in 2009 (top panel) and 2010 (bottom panel) as a function of ecliptic longitude of *IBEX*, corrected for ionization along the trajectory, and for observation of differential flux vs. distribution function (see the text). Also shown are the peak positions with uncertainty and the sigmas of the width as deduced from a least-squares fit of the data points to a Gaussian distribution.

(A color version of this figure is available in the online journal.)

already integrates over the entire distribution in velocity space (Lee et al. 2012).

Figure 6 shows the rates corrected for ionization and for the speed bias discussed above as a function of ecliptic longitude of the observer at the "Sun-pointing location" for each *IBEX* orbit in 2009 (left panel) and 2010 (right panel). We fitted the resulting data points with a Gaussian in ecliptic longitude to determine the position of the ISM flow peak and found $\lambda_{\rm Peak} = 130.^\circ6 \pm 0.^\circ7$ (the only observable parameter in Equations (1) and (2)) as the combined 2009 and 2010 value with all uncertainties included. As shown in Figure 6, the fitted values for 2009 and 2010 are almost identical, well within the uncertainties for the peak determination, as also shown in Figure 6. This analysis yields the location in ecliptic longitude in Earth's orbit where the trajectories of the interstellar He bulk flow reach their perihelion. Accidentally, the peak ISM flow is observed close to perihelion of the Earth. To account for the slightly enhanced acceleration of the ISM flow and the increased speed of the Earth, we use the actual distance of the Earth from the Sun in our analysis rather than the average distance.

4. DETERMINATION OF THE INFLOW LATITUDE AND TEMPERATURE OF He AS A FUNCTION OF $\lambda_{\rm ISM\infty}$

In the previous section, we found a relation between the inflow direction $\lambda_{\rm ISM\infty}$ and the bulk speed $V_{\rm ISM\infty}$ of the interstellar gas

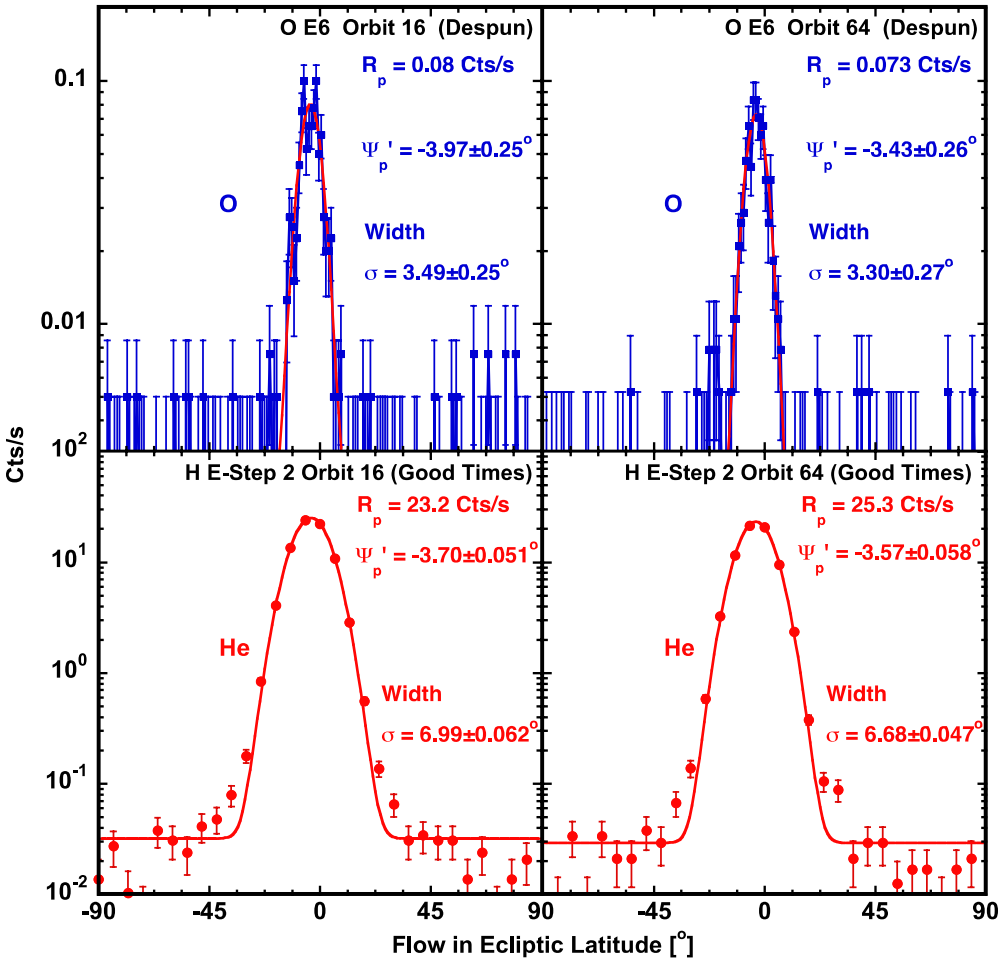

Figure 7. Angular distribution in ecliptic latitude of interstellar He (lower two panels) and of O with an admixture of Ne (upper two panels) for orbits 16 (left panels) and 64 (right panels). The He (O + Ne) distributions are shown in 6° (1° because of the narrower peaks) bins, based on the present analysis. Also shown is the Gaussian for each distribution that was found with maximum likelihood fitting at the given parameters, which includes de-convolution of the collimator function (see the text).

based on the longitude where the ISM flow maximum is actually observed. As derived by Lee et al. (2012), Equations (3) and (4) now connect the peak location $\psi'_{\rm Peak}$ of the flow distribution in latitude (or in spin phase for the IBEX-Lo observation), obtained at the longitude of maximum ISM flow, with the latitudinal inflow angle of the ISM at infinity, $\beta_{\rm ISM\infty}$. Since both $\lambda_{\rm ISM\infty}$ and $V_{\rm ISM\infty}$ are involved in these relations, $\beta_{\rm ISM\infty}$ is also determined as a function of $\lambda_{\rm ISM\infty}$.

4.1. Determination of Peak Location and Width of the ISM Flow in Latitude

The Mach number of the ISM flow and thus its temperature is determined from σ'_ψ, which is obtained from a maximum likelihood fit to an assumed Gaussian distribution of the observed flow distribution in latitude, deriving the corresponding values in the ISM flow using again Equations (3) and (4). We find the angles in ψ' that represent the $1/e$ points of the observed distributions in latitude by adding and subtracting σ'_ψ to $\psi'_{\rm Peak}$. Using the same procedure as for $\psi'_{\rm Peak}$, we translate these points into the ISM distribution at infinity, finding the $1/e$ points of the ISM flow distribution and thus σ_∞. This value can then be readily translated into the flow Mach number at infinity, $M_{\rm ISM\infty}$. Finally, the temperature is derived using $M_{\rm ISM\infty} = V_{\rm ISM\infty}/C_\infty$, where C_∞ is the sound speed. Again, using the same arguments as just discussed at the beginning of this section, the Mach number and the temperature are also functions of the inflow longitude of the ISM flow, i.e., $M_{\rm ISM\infty}(\lambda_{\rm ISM\infty})$ and $T(\lambda_{\rm ISM\infty})$. Because it is straightforward to relate σ'_ψ and $\psi'_{\rm Peak}$ at the ISM flow maximum to the temperature T and the inflow latitude, $\beta_{\rm ISM\infty}$, at infinity, we start the analysis using these observed parameters.

Figure 7 shows the angular distributions in ecliptic latitude of the ISM flow for He in energy step 2 and O + Ne in energy steps 5 + 6 as obtained for orbit 16 in 2009 and orbit 64 in 2010, i.e., the orbits closest to the ISM flow peak. The He distributions are integrated over the "good" times as specified in Table 1, accumulated in 6° bins, and corrected for the onboard histogram data. For O + Ne, 1° binning is used because of the substantially narrower flow distribution of these higher mass species. Because the count rate for these species is so much lower, we are making use of the entire accumulation periods of the data, including the times when the distributions had to be de-spun because the star tracker was blinded. To account for potential inaccuracies in the current de-spinning method, an additional systematic uncertainty of ±0.°2 is added quadratically to the respective uncertainties in σ'_ψ and $\psi'_{\rm Peak}$.

σ'_ψ and $\psi'_{\rm Peak}$ are determined by fitting of a Gaussian distribution to the angular distributions using a maximum likelihood fitting procedure that treats height, peak location, and σ-width of the Gaussian, as well as a homogenous background, as free parameters. The known FoV function of IBEX-Lo is built into the algorithm as a convolution over the source distribution so

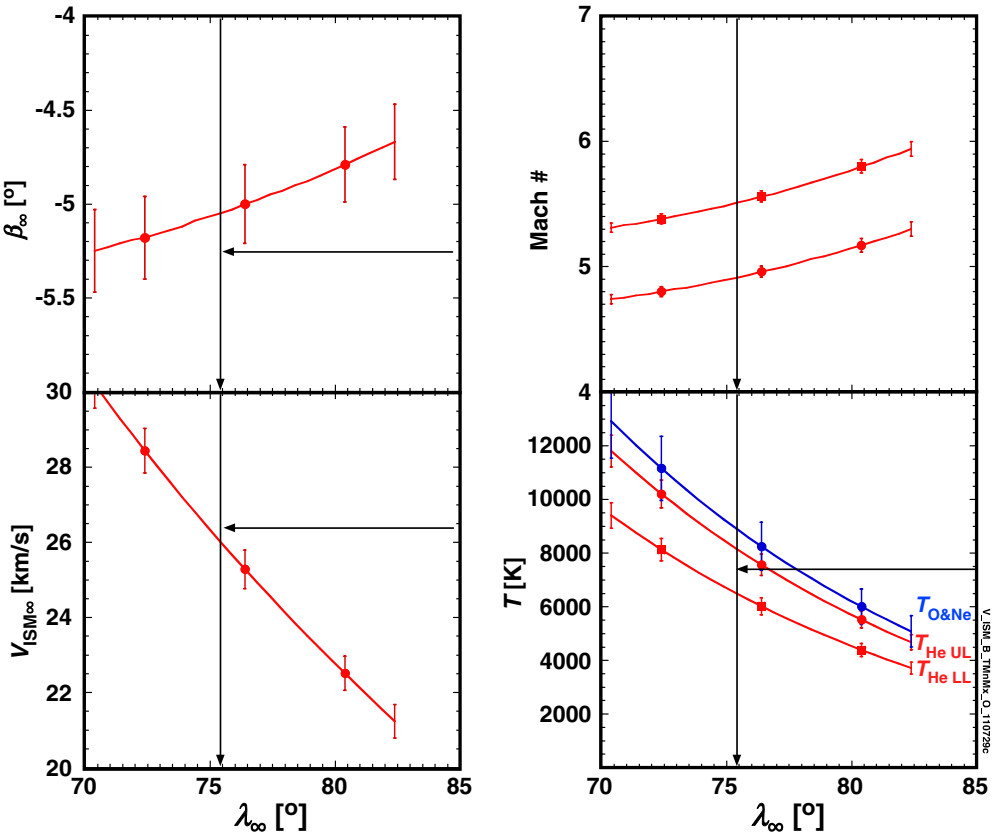

Figure 8. Interstellar He flow parameters as a function of inflow longitude λ_∞ outside the heliosphere based on the ecliptic longitude of the ISM flow maximum at 1 AU of 130.°6 ± 0.°6 and the measurement of the peak latitude and width of the flow at the ISM flow maximum. Shown are the ISM flow speed $V_{ISM\infty}$ (lower left panel), the inflow latitude β_∞ (upper left panel), the Mach number of the flow (upper right panel) for He, and the temperature T for both He (red curves) and the O + Ne combination (blue curve; lower right panel). The lines with arrows indicate the ISM parameters found by Witte (2004). The peak and width in latitude have been obtained from a linear interpolation between the values obtained for orbits 15 and 16 as well as 63 and 64 based on the Sun-pointing locations at the beginning of the orbits and the longitude of the ISM flow maximum. For the He temperature determination, the width of the observed distribution was corrected for the minimum ($T_{He\ UL}$) and the maximum ($T_{He\ LL}$) rate-dependent suppression of events, as described in the text. For the O + Ne temperature such correction is not necessary because of the much lower count rates.

that the net width of the distribution is returned. Figure 7 shows the resulting Gaussian as a solid curve along with the fit parameters and their uncertainties resulting from the fit. Because peak height, ψ'_{Peak}, and σ'_ψ vary only very little close to the ISM flow maximum, the average values over the good times of orbits 16 and 64 are used in lieu of an extrapolation to the "Sun-pointing location." This procedure is justified by a flat behavior of all parameters in orbit 64, with "good" data over an extended time period.

However, the location of the ISM flow peak at 1 AU does not exactly coincide with the "Sun-pointing location" in orbit 16 or 64, but rather falls between the locations of orbits 16 and 15 as well as 64 and 63, respectively. Therefore, we apply a small correction to the values of ψ'_{Peak} and σ'_ψ that are obtained from orbits 16 and 64 based on the previous orbits and the distance of the "Sun-pointing locations" from the ISM flow maximum location for the analysis of $\beta_{ISM\infty}$ and T in Section 4.2. As can also be seen from Figure 7, the values obtained for He and O in both years agree with each other very well.

Because we relate all our analysis to the perihelion of the ISM flow at 1 AU, the same inter(extra)polation procedure, described in Section 3 for the peak rates, is used here to determine the peak location in latitude, ψ'_{Peak}, for all other orbits outside the ISM flow peak. Since ψ'_{Peak} as a function of observer longitude will be used in Section 5, we performed this analysis for all orbits that are suitable for extrapolation, as noted in the last column of Table 1.

4.2. ISM Flow Parameter Sets as a Function of Inflow Longitude at Infinity

We deduced $V_{ISM\infty}(\lambda_{ISM\infty})$, $\beta_{ISM\infty}(\lambda_{ISM\infty})$, $M_{ISM\infty}(\lambda_{ISM\infty})$, and $T(\lambda_{ISM\infty})$ using the above-mentioned analysis to determine the location of the ISM flow maximum in ecliptic longitude and the peak position and sigma of the angular flow distribution in latitude at the peak maximum. Figure 8 shows these ISM flow parameters as a function of $\lambda_{ISM\infty}$ in a four-panel compilation over a range in $\lambda_{ISM\infty}$ from 70° to 83°. Uncertainties are obtained as follows. For the uncertainty of $\lambda_{ISM\infty}$, we have quadratically combined the uncertainty derived from the fit to the longitudinal distribution with the uncertainties of the center of mass of the distribution from data points of the individual orbits. Finally, we added ±0.°2 because of uncertainties in the flow aberration. The uncertainty in $V_{ISM\infty}$ is obtained through the slope of $V_{ISM\infty}(\lambda_{ISM\infty})$ from the uncertainty in $\lambda_{ISM\infty}$ as described above. For $\beta_{ISM\infty}$ $(\lambda_{ISM\infty})$, the uncertainty for ψ'_{Peak} is first determined in a similar way to that for $\lambda_{ISM\infty}$. This uncertainty is translated into that for $\beta_{ISM\infty}$ by error propagation and combined quadratically with the uncertainty for $\lambda_{ISM\infty}$. As discussed above, the main source of uncertainty for $M_{ISM\infty}(\lambda_{ISM\infty})$ and $T(\lambda_{ISM\infty})$ is the rate-dependent event

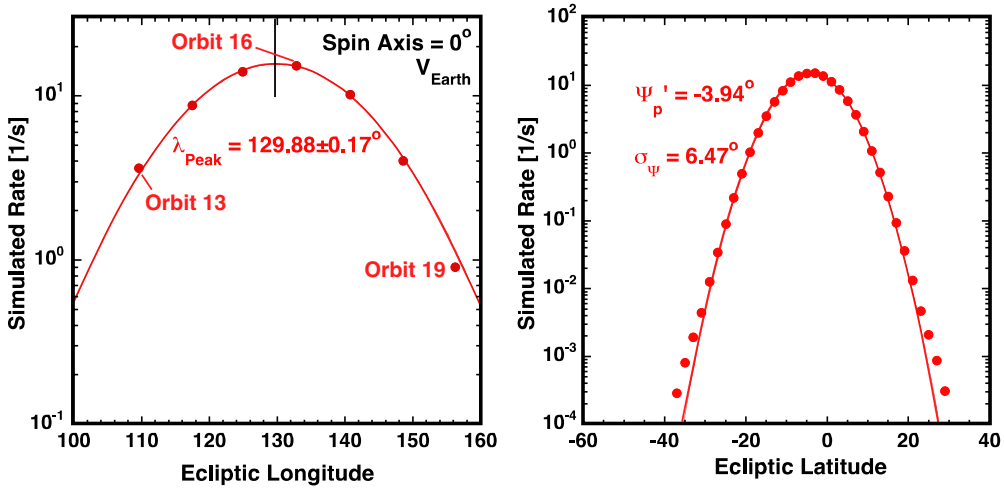

Figure 9. ISM flow rate for He, corrected for ionization loss (after integrating the simulated phase-space densities to obtain fluxes), as a function of ecliptic longitude (left panel) and ecliptic latitude in the peak orbit 16 (right panel) using test particle simulations as input (Bzowski et al. 2012) for the location of exact Sun-pointing of the *IBEX* spin axis in each orbit.

(A color version of this figure is available in the online journal.)

throughput in the CEU, which is currently not fully quantified. Therefore, we present two estimates for these parameters for the minimum and maximum estimated equivalent CEU processing time. A description of the current understanding of how the rate-dependent CEU throughput likely affects the temperature determination and how we have arrived at the estimates for an approximate correction can be found in Appendix B. Of course, the temperature estimates also carry the uncertainty in $\lambda_{\mathrm{ISM}\infty}$. As a result, we obtain a rather well-constrained ISM flow vector as a function of $\lambda_{\mathrm{ISM}\infty}$, with $\lambda_{\mathrm{ISM}\infty}$ known to $\pm 0.^{\circ}7$, where $V_{\mathrm{ISM}\infty}$ is within ± 0.5 km s^{-1} and $\beta_{\mathrm{ISM}\infty}$ within $\pm 0.^{\circ}2$ for a given $\lambda_{\mathrm{ISM}\infty}$, with larger uncertainties for the temperature.

As described above, Figure 7 also shows the latitudinal flow distribution for the combination of interstellar O + Ne (see Bochsler et al. 2012 for the observed Ne/O ratio). Because the count rate for these species is much lower than that for He, we use the entire accumulation periods of the data, including the times when the distributions had to be de-spun because the star tracker was blinded, to compare the peak locations of O + Ne with those of He. We estimate an additional contribution to the error of the peak location and width of the order of $\pm 0.^{\circ}2$, which we also add quadratically to the statistical uncertainties. Given these uncertainties, the peak locations of O + Ne from the two years agree with each other and with that of He. Therefore, it can be concluded that the ISM flow directions of these species are identical within observational uncertainties.

The observed angular width of O + Ne (the collimator FoV is taken into account in the maximum likelihood analysis) is substantially lower than that for the He distribution. This is due to the substantially higher mass of O and Ne and the fact that the angular distribution essentially reflects the flow Mach number at infinity. To derive the temperature from the related velocity distribution, we take into account a 14% admixture of Ne in the observed distribution in the detector system, which translates into an Ne/O ratio of 0.4 at the observer location after taking into account detection efficiencies (Bochsler et al. 2012). This leads to an effective mass of 16.55 for the combination, from which we obtain a temperature in the range of 5300–9000 K that is again a function of $\lambda_{\mathrm{ISM}\infty}$ (included along with error bar in the lower right panel of Figure 8).

4.3. Comparison of the Analytical Method with a Test Particle Simulation

To further test the validity of our approach and to directly compare the results obtained using the analytical method (this paper) with those based on a test particle approach (Bzowski et al. 2012), a specific set of test particle simulations was performed. This set produces the predicted IBEX-Lo count rates and latitudinal flow distributions at the "Sun-pointing location" for orbits 13–19. For this comparison, we chose ISM flow vector values given by Witte (2004), i.e., $\lambda_{\mathrm{ISM}\infty} = 75.^{\circ}4$ (Note that Witte (2004) used B1950 coordinates in his paper, for which $\lambda_{\mathrm{ISM}\infty} = 74.^{\circ}5$ (M. Witte 2010, private communication), while we use J2000 coordinates, for which $\lambda_{\mathrm{ISM}\infty} = 75.^{\circ}4$), $\beta_{\mathrm{ISM}\infty} = -5.^{\circ}31$, $V_{\mathrm{ISM}\infty} = 26.4$ km s^{-1}, and ISM temperature $T = 6320$ K. Further, we assume that the spin axis is oriented exactly in the ecliptic and that the spacecraft is at rest relative to the Earth. In this way, we were able to apply our analytic method described above using the simulated data set without any further corrections.

Figure 9 (left panel) shows the simulated ISM flow rates at the "Sun-pointing location" in each orbit after correction for ionization loss and taking into account the fact that particle flux (rather than phase-space density) is observed. A Gaussian fit to this longitudinal distribution is also shown as a solid curve. In the right panel of Figure 9, the simulated flow distribution in latitude is displayed for the "Sun-pointing location" in orbit 16 along with its Gaussian fit. Again, we derive $V_{\mathrm{ISM}\infty}(\lambda_{\mathrm{ISM}\infty})$ from the maximum in longitude. After adopting the inflow longitude $\lambda_{\mathrm{ISM}\infty} = 75.^{\circ}4$ (Witte 2004), we find $V_{\mathrm{ISM}\infty} = 25.5 \pm 0.3$ km s^{-1}, and from the peak and width of the latitudinal distribution of the simulated orbit 16 we obtain $\beta_{\mathrm{ISM}\infty} = -5.34 \pm 0.^{\circ}03$ and $T = 6150 \pm 200$ K, i.e., in reasonably good agreement with the original parameters that went into the test particle simulations.

The fact that the ISM flow speed we obtain with the analytical method is lower by about 0.9 km s^{-1}, i.e., slightly outside the 1σ uncertainty derived from observations, may in part be due to simplifications used in the analytical method. For example, we obtain the ISM peak location in longitude from the simulated observations as if the sensor had an infinitely narrow FoV. Because of the asymmetry in the way the cuts

through the distribution function change with orbits over the peak, there is a slight shift in the peak location. In addition, we use an average ionization rate, while the test particle model tracks all temporal changes. It should also be pointed out that the latitudinal distributions of the simulated observation are represented by a Gaussian only to about 5% of the peak rate level and then deviate, showing elevated wings, in particular in orbits closer to the gravitational focusing cone. Most importantly, while the ISM inflow distribution at infinity is assumed to be a Maxwellian that is convected with the ISM flow speed (Bzowski et al. 2012), the effect of the Sun's gravitational potential distorts the original Gaussian distribution, especially far away from the ISM flow peak at 1 AU (Lee et al. 2012). This also leads to a small asymmetry in the longitude distribution with a slight elevation of the downwind over the upwind wing. A progressive reduction in the number of input points toward the center in the fit showed that this asymmetry leads to a shift in the ISM flow peak location toward smaller longitudes. The resulting shift in the corrected peak location is at most 0.°4 with respect to that obtained from the Gaussian fit, thus leading to a higher deduced inflow speed (closer to the input value for the simulations) and a somewhat better fit to the simulated data. At this stage, we include an independent additional systematic uncertainty of 0.°4 in the results for $\lambda_{ISM\infty}$. Overall, the original ISM flow parameters that were used as input for the test particle simulations are retrieved to a reasonably good accuracy using our analytical method.

5. CONSTRAINTS ON THE ISM INFLOW VECTOR

So far, we have derived the ISM flow parameters as a function of the inflow direction at infinity in ecliptic longitude $\lambda_{ISM\infty}$. Without further information, this degeneracy cannot be eliminated, except that choices of $\lambda_{ISM\infty} < 70^\circ$ and $\lambda_{ISM\infty} > 84^\circ$ would lead to unrealistically high (>30 km s^{-1}) or low (<20 km s^{-1}) values for the ISM flow speed, respectively. As discussed in Lee et al. (2012), there are two additional observables in the ISM flow at 1 AU that can be used to further constrain the value for $\lambda_{ISM\infty}$. First, the observed peak location of the ISM flow distribution in latitude ψ'_{Peak}, which is related to the inflow angle in latitude at infinity $\beta_{ISM\infty}$ (which in turn depends on the observer longitude), also varies with the actual ISM flow speed observed at 1 AU, i.e., depends explicitly on $V_{ISM\infty}$ and thus on $\lambda_{ISM\infty}$. Second, around the location of the ISM flow maximum at 1 AU, the ratio of the angular width of this distribution in longitude and latitude, i.e., $\sigma_\lambda/\sigma_\psi$, depends largely on the inflow speed at infinity $V_{ISM\infty}$, with some influence from the ISM temperature (Lee et al. 2012). Therefore, the peak position in latitude as a function of observer longitude and the ratio of the sigma widths can be used to further constrain $V_{ISM\infty}$ and $\lambda_{ISM\infty}$.

5.1. Variation of the Flow Peak in Latitude as a Function of Observer Longitude

As can be seen from Equations (1), (3), and (4), for a set $\beta_{ISM\infty}$, the peak of the ISM flow distribution in latitude, ψ'_{Peak}, that is observed during a specific orbit also depends on the observer longitude, λ_{Obs}, while the degree of this variation also depends on the value of $V_{ISM\infty}$ relative to Earth's speed V_E. The latter is a consequence of the transformation of the flow between the rest frame and the observer frame given in Equation (4). While the application of Equations (1) and (3) is straightforward, the frame transformation given in Equation (4) also depends on the actual portion of the ISM velocity distribution that is sampled by IBEX-Lo in each orbit, i.e., on the specific observer longitude λ_{Obs}.

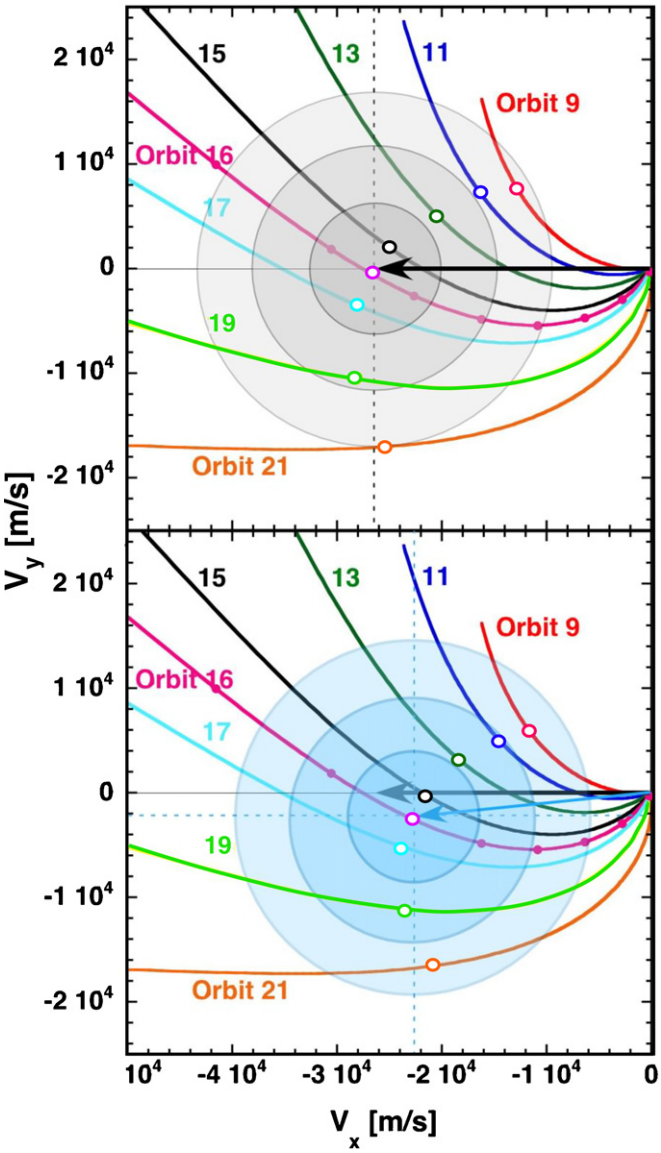

Figure 10. Cuts through the ISM flow velocity distribution in the ecliptic plane at infinity, as sampled by IBEX-Lo at 1 AU during the indicated orbits for the "Sun-pointing location" (solid colored lines). The velocity distributions at infinity are shown for $V_{ISM\infty} = 26.4$ km s^{-1} and $\lambda_{ISM\infty} = 75.°4$ (top panel) and for $V_{ISM\infty} = 22.5$ km s^{-1} and $\lambda_{ISM\infty} = 81.°2$ (bottom panel), with the x-axis oriented along the inflow vector with $\lambda_{ISM\infty} = 75.°4$ (black arrow) in both panels.

Figure 10 shows cuts through simulated ISM flow distributions at infinity in the ecliptic plane for two different sets of flow parameters, i.e., $\lambda_{ISM\infty} = 75.°4/81.°2$ and $V_{ISM\infty} = 26.4/22.5$ km s^{-1}, respectively. The x-axis in both panels is the ISM inflow direction for the case with $\lambda_{ISM\infty} = 75.°4$. The phase-space density is indicated with different shading in concentric circles. Also shown are curves that are computed using Equations (1) and (2), which relate V_∞ to λ_∞ at the "Sun-pointing location" for each of the indicated *IBEX* orbits. Note that Equation (2) applies not just to the ISM bulk flow but also to any ISM atom trajectory that arrives at its perihelion at λ_{Obs}. Therefore, the respective curves in Figure 10 represent a cut through the neutral atom velocity distribution in the ecliptic

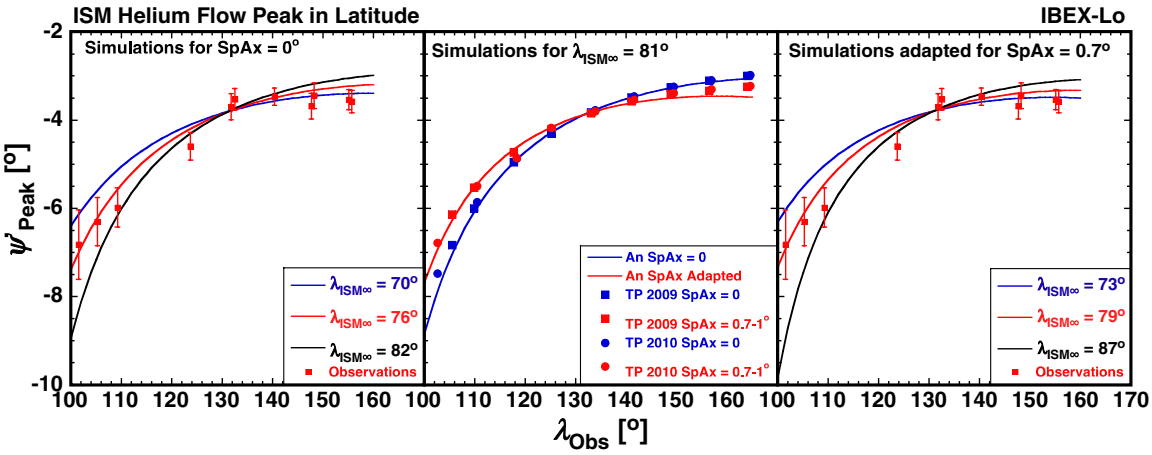

Figure 11. Latitude $\psi'_{\rm Peak}$ of the He ISM flow peak as a function of observer longitude $\lambda_{\rm Obs}$. Left panel: observed values for $\psi'_{\rm Peak}$, along with measurement uncertainties, from 2009 and 2010 along with analytical curves for $\lambda_{\rm ISM\infty} = 70°$, 76°, and 82° computed for cases when the spin axis is exactly in the ecliptic. Center panel: analytical curve $\psi'_{\rm Peak}(\lambda_{\rm Obs})$ with the spin axis in the ecliptic (blue curve) and adapted for the spin axis at $+0.^{\circ}7$ latitude (red curve) along with results from test particle modeling (Bzowski et al. 2012) for the spin axis in the ecliptic (blue symbols) and for actual *IBEX* spin-axis orientations (red symbols). Right panel: same as the left panel, but with the analytical curves for $\lambda_{\rm ISM\infty} = 73°$, 79°, and 85° adapted for the spin axis at $+0.^{\circ}7$ latitude.

plane that is sampled in a specific orbit. This cut includes vastly different speeds and thus energies. However, because IBEX-Lo utilizes sputtered ions from the incoming He atoms for identification of He, the *IBEX* observation represents an integral flux over all energies up to the maximum energy (see Figure 1). Because the distribution in the ISM is presumably symmetric around the bulk velocity vector and strongly peaked, the bulk flow vector for each such cut may be represented by the center of mass along these curves in velocity space, which falls on the maximum phase-space density on each curve. The open circles in the respective color of each orbit indicate these locations on the distribution. It should be noted that a correction similar to that used in Section 3 is applied here to account for the fact that IBEX-Lo measures differential flux rather than phase-space density. The velocities at these maxima have been computed through numerical integration over the velocity distribution as well as analytically, as discussed by Lee et al. (2012).

In Figure 11, we show the observed ISM flow peak angles in latitude, $\psi'_{\rm Peak}$ (with measurement uncertainties), as a function of observer longitude, $\lambda_{\rm Obs}$, for the "Sun-pointing locations" in each orbit for 2009 and 2010. For comparison, $\psi'_{\rm Peak}(\lambda_{\rm Obs})$ as obtained using our analytical calculation is also shown for several sets of ISM flow conditions, with $\lambda_{\rm ISM\infty}$ being a parameter. In the left panel, a simplified analytical solution is shown for the case of the *IBEX* spin axis lying exactly in the ecliptic plane. (Note, however, that the spin axis actually points in the range of $+0.^{\circ}7 < \delta < +1.^{\circ}0$ ecliptic latitude.) The center panel of Figure 11 shows test particle simulations for $\psi'_{\rm Peak}(\lambda_{\rm Obs})$ with the spin axis lying in the ecliptic (blue symbols) and with the actual *IBEX* orientation for each orbit (red symbols) along with the analytical solution for the spin axis exactly in the ecliptic (blue curve) and a solution that is adapted for actual spin-axis pointing, parameterized in δ (red curve). As can be seen from the test particle simulations (Bzowski et al. 2012), differences in $\psi'_{\rm Peak}(\lambda_{\rm Obs})$ due to the spin-axis orientation are significant. Both cases agree well with the analytical relation for similar spin-axis orientation. No orbit-to-orbit variation was included in the analytical solution, and $\delta = +0.^{\circ}7$ was used. The right panel of Figure 11 shows the observed ISM flow peak angles together with the modified analytical solution for a spin-axis orientation, $\delta = +0.^{\circ}7$, in a similar representation as in the left panel.

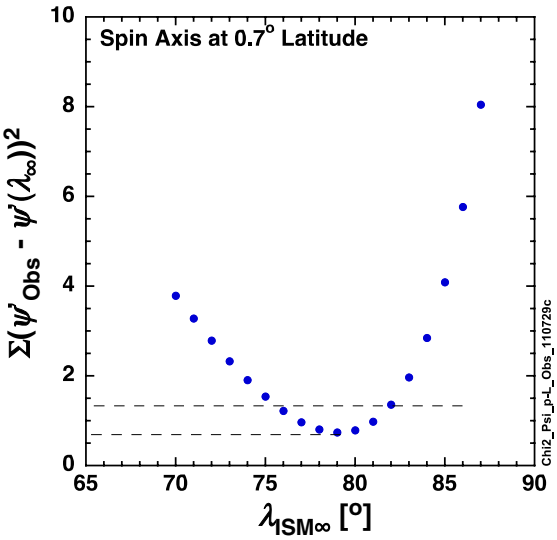

Figure 12. Sum of the squared deviations (χ^2) of the observations from the analytical $\psi'_{\rm Peak}(\lambda_{\rm Obs})$ taken from the right panel of Figure 11 for different values of $\lambda_{\rm ISM\infty}$. The minimum χ^2 is found at $\lambda_{\rm ISM\infty} = 79°$, with the χ^2 at twice the minimum value at $75.^{\circ}5$ and 82°, respectively.

To find the optimum value for $\lambda_{\rm ISM\infty}$, the analytical relation $\psi'_{\rm Peak}(\lambda_{\rm Obs})$ was evaluated using the sum of the squares of the deviation between the analytical curve and the observed $\psi'_{\rm Peak}$ values (i.e., χ^2), with $\lambda_{\rm ISM\infty}$ as a variable parameter. The results are shown in Figure 12 for the analytic solution with $\delta = 0.^{\circ}7$ and $\lambda_{\rm ISM\infty}$ incremented by 1° steps. Minimum χ^2 is at $\lambda_{\rm ISM\infty} = 79°$, with χ^2 doubling at $75.^{\circ}5$ and 82°, respectively. We have adopted the condition that the value doubles from its minimum to define a conservative 1σ uncertainty of $\lambda_{\rm ISM\infty}$. This also seems justified because the averaged uncertainty squares of the observed $\psi'_{\rm Peak}$ are somewhat smaller than the minimum. As a result, the optimum range for the inflow longitude appears to be $\lambda_{\rm ISM\infty} = 79 + 3.^{\circ}0(-3.^{\circ}5)$.

5.2. Ratio of the Width of the Flow Distribution in Longitude and Latitude

Lee et al. (2012), showed that $\sigma_\lambda/\sigma_\psi(V_{\rm ISM\infty})$ starts at 0, has a broad maximum with values around 1.7–1.85 over a

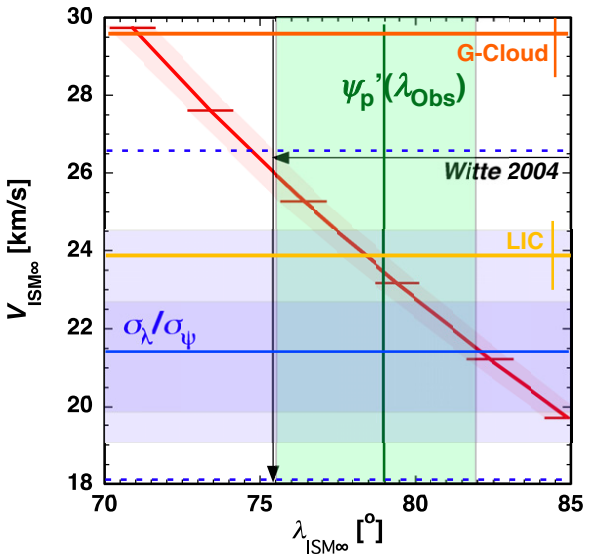

Figure 13. $V_{ISM\infty}$ as a function of $\lambda_{ISM\infty}$ (solid red line) derived in this paper with measurement uncertainty (error bars and pink shaded region). Also shown are the constraints placed on $\lambda_{ISM\infty}$ by the observation of $\psi'_{Peak}(\lambda_{Obs})$ (solid green line) with measurement uncertainty (green shaded region) and on $V_{ISM\infty}$ by $\sigma_\lambda/\sigma_\psi$ at the ISM flow maximum (solid blue line) with measurement uncertainties. The dark blue region indicates the uncertainty introduced solely by the current temperature uncertainty, the light blue region is solely due to the uncertainty in the sigma ratio, and the dashed blue lines give full uncertainties for both effects combined. For comparison, values obtained by Witte (2004; black arrows) and the velocities of the LIC (yellow) and the G-Cloud (brown) given by Redfield & Linsky (2008) are included.

reasonable temperature range, and then decreases to 1 for $V_{ISM\infty} \rightarrow \infty$. From the variation of the ISM flow as a function of λ_{Obs} (Figure 6) we also obtained the width in longitude $\sigma_\lambda = 11.^\circ9 \pm 0.^\circ6$, and from the latitudinal distribution at the flow maximum (Figure 7) we obtained the width in latitude $\sigma_\psi = 7.^\circ42 \pm 0.^\circ25$ averaged over both the 2009 and 2010 observing seasons, resulting in a ratio $\sigma_\lambda/\sigma_\psi = 1.60 \pm 0.097$. Lee et al. (2012) computed the observed ratio after integrating over the instrument FoV. Therefore, the ratio is taken directly from the observed sigmas, without including a de-convolution of the FoV. In principle, there are two resulting values of $V_{ISM\infty}$ for this ratio. However, inflow speed values beyond the maximum are unreasonably high and thus unphysical. Based on the sigma ratio and using the temperature value in the curve in the lower right panel of Figure 8 for the minimum data-loss correction (red circles, annotated $T_{He\ UL}$) for the optimum value of $\lambda_{ISM\infty}$ found in Section 5.1 ($T_{He} = 6200$ K), we derive a value of $V_{ISM\infty} = 21.4$ km s^{-1}. Lee et al. (2012, Figure 5) have shown that $\sigma_\lambda/\sigma_\psi(V_{ISM\infty})$ still contains a moderate temperature dependence, which is taken into account through a family of curves in their analysis. Taking into account the full temperature range, given in the two curves in the lower right panel of Figure 8 for the uncertainty in $\lambda_{ISM\infty}$ from Section 5.1, leads only to a narrow range of possible values for $V_{ISM\infty}$ because the ratio of the two widths is involved. However, adding full measurement error propagation for the ratio of the sigmas leads to a sizeable uncertainty.

5.3. Combination of the Two Constraints

Figure 13 shows the ISM inflow speed $V_{ISM\infty}$ as a function of $\lambda_{ISM\infty}$ taken from the bottom left panel of Figure 8. The most likely range of $\lambda_{ISM\infty}$ (from the flow peak in latitude as a function of observer longitude $\psi'_{Peak}(\lambda_{Obs})$) and the range of $V_{ISM\infty}$ (from the analysis of the ratio $\sigma_\lambda/\sigma_\psi$) are included as transparent green and blue regions in Figure 13, along with lines for the center values. The narrow dark blue shaded rectangle for the sigma ratio indicates the possible range in $V_{ISM\infty}$ for the temperature variation over the range in $\lambda_{ISM\infty}$ from Section 5.1 for the center value $\sigma_\lambda/\sigma_\psi = 1.60$, while the light blue rectangle reflects the $\sigma_\lambda/\sigma_\psi$ error bar given above for the center temperature value of 6200 K. Combining these two uncertainties in the observations leads to the wider limits indicated by the two horizontal dashed blue lines. As a result, the blue dashed horizontal line just above 26.5 km s^{-1} is the upper limit for allowable $V_{ISM\infty}$. The wider range in $V_{ISM\infty}$, allowed by the sigma ratio condition, completely includes the possible range from the condition placed by the observed peak position in latitude. The combination of these two independent conditions provides a consistent range for $\lambda_{ISM\infty}$ and $V_{ISM\infty}$, with $\lambda_{ISM\infty} = 75.^\circ5$–$82^\circ$. The fact that the triangle formed by the three center value lines (red, green, and blue) in Figure 13 covers a range in $\lambda_{ISM\infty}$ of $\approx 3^\circ$ can be attributed to the width of the current measurement uncertainties.

Following the arguments in Section 2.3 and as shown in Figure 8, $\beta_{ISM\infty}$, $M_{ISM\infty}$, and T are also unique functions of $\lambda_{ISM\infty}$. Thus, these parameters are constrained by the same range in $\lambda_{ISM\infty}$. Combining these results, we get $V_{ISM\infty} = 21.5$–26.5 km s^{-1}, $\beta_{ISM\infty} = -4.^\circ6$ to $5.^\circ3$, $M_{ISM\infty} = 4.8$–5.3, and $T_{He} = 5000$–8200 K (for the minimum data-loss correction). As indicated before, the ISM flow vector is narrowly constrained as a function of $\lambda_{ISM\infty}$, while at this point there is still a large uncertainty of the temperature.

6. DISCUSSION AND CONCLUSIONS

In this paper, we have determined a set of interstellar flow parameters for He from interstellar neutral gas observations at 1 AU for the first time, using IBEX-Lo ISM flow observations in the winter/spring seasons of 2009 and 2010. In addition, we have obtained, for the first time, the latitudinal inflow angle and the temperature for a combination of interstellar O and Ne that is observed at 1 AU (Bochsler et al. 2012). The O + Ne flow maximum occurs during the same *IBEX* orbit as does the He maximum. This result is consistent with the same inflow longitude and ISM flow speed for all three species, although a more accurate determination requires a more detailed analysis. The O + Ne peak location in latitude is in very close agreement with that of He, within the observational uncertainties. These results imply that the ISM flow vector is the same for these species and that the flow is collisionally equilibrated.

Here, we applied an analytical approach, using data only from time periods when the ISM flow trajectories were close to their perihelion. First, we determined a rather tight functional dependence between $V_{ISM\infty}$ and $\lambda_{ISM\infty}$ using the longitude of the ISM flow maximum. Then we obtained $\beta_{ISM\infty}$ and T separately from the peak location and width of the angular flow distribution in latitude at the flow maximum, again as a function of $\lambda_{ISM\infty}$. We constrained $\lambda_{ISM\infty}$ to $79 + 3(-3.^\circ5)$, making use of two equations derived in Lee et al. (2012), e.g., $\psi'_{Peak}(\lambda_{Obs})$, which parameterizes in $\lambda_{ISM\infty}$, and $\sigma_\lambda/\sigma_\psi(V_{ISM\infty})$, which only shows a reduced dependence on T. Following this method, we determined all ISM flow parameters, one at a time, rather than finding the entire best set at once using a multi-parameter optimization method, which is needed when a test particle simulation is compared to *IBEX* observations (Bzowski et al. 2012). Our values closely match those determined by Bzowski et al. (2012), who found $\lambda_{ISM\infty} = 79.^\circ2$, $V_{ISM\infty} = 22.8$ km s^{-1},

$\beta_{ISM\infty} = -5.^{\circ}1$, and $T_{He} = 6200$ K as an optimum parameter set from minimizing χ^2 between model predictions and *IBEX* observations. They find, as we do here with our analytical analysis, that $V_{ISM\infty}$, $\beta_{ISM\infty}$, and T_{He} are functionally related to $\lambda_{ISM\infty}$ and constrain their $\lambda_{ISM\infty}$ to the range $75.^{\circ}5$–83°. This result is also consistent with a direct comparison of the test particle simulations with our analytical approach for simulated data as discussed in Section 4.3. Observations one year apart (2009 and 2010) lead to nearly identical values for all parameters, as well as for the observed maximum rate, which was only 15% lower in 2010 compared with 2009 at the peak location. This very close match in the maximum observed rate is most likely due to the extended solar minimum over the past few years (e.g., McComas et al. 2008), with the He ionization rate only up by ≈10% in 2009 over 2008 (Bzowski et al. 2012). This also implies that detection efficiencies of IBEX-Lo have been very stable.

Our analysis of the IBEX-Lo neutral gas observations at 1 AU gives somewhat different values for the inflow longitude and the ISM flow speed when compared with the previous determination, which combined *Ulysses* neutral gas observations (Witte 2004), UV backscattering observations (Lallement et al. 2004; Vallerga et al. 2004), and pickup ion observations (Gloeckler et al. 2004) during solar maximum. The consensus values based on the earlier observations were $\lambda_{ISM\infty} = 75.^{\circ}4$ (in J2000) and $V_{ISM\infty} = 26.4$ km s^{-1} (Möbius et al. 2004), largely determined by the neutral gas observations (Witte 2004) owing to their small uncertainties. These values are still very close to the $V_{ISM\infty}(\lambda_{ISM\infty})$ relation determined from the IBEX-Lo observations, but at the edge of the current 1σ error band for both constraining conditions (cf. Figure 13, which also shows the values of Witte 2004). The flow directions in latitude of the 2004 consensus values and this new determination are in close agreement. The temperature determination using *IBEX* data still carries a large uncertainty and overlaps with the earlier consensus values. However, the most likely values for the flow direction in longitude and the ISM flow speed based on analysis of *IBEX* data given here appear different by $\approx 3.^{\circ}5$ and ≈3.5 km s^{-1}, respectively, from the 2004 consensus parameters. Including the relatively large uncertainty that still must be placed on the $\lambda_{ISM\infty}$ determination, the 2004 consensus values fall just at the edge of the uncertainty band obtained from the variation of the inflow direction in latitude over observer longitude.

Finally, we present some ideas on the possible differences. For the derivation of the flow parameters from the *Ulysses* GAS observations a multi-parameter optimization was performed. This procedure included the ionization rate and the neutral He density at the termination shock as free parameters (Banaszkiewicz et al. 1996). *Ulysses* observations were made largely at distances >1.5 from the Sun and at ≈90° from the inflow direction, i.e., before perihelion, where gravitational deflection is considerably weaker than at 1 AU. This deflection is used to deduce the flow speed from its arrival direction. The UV backscatter observations generally have somewhat larger uncertainties. The fact that the pickup ion observations (Gloeckler et al. 2004) appeared to indicate an alignment of the gravitational focusing cone at 1 AU with the flow direction as derived by Witte (2004) should not be overinterpreted. Möbius et al. (2004) indicated that this co-alignment could mean that the average cone location in the pickup ions is not influenced greatly by interplanetary conditions. However, recent observations of the focusing cone with *STEREO* PLASTIC (Möbius et al. 2010) indicated that the observed spatial variation of pickup ions is largely determined by solar wind stream structures. A difference in the cone location as seen in pickup ions relative to the neutral gas inflow direction could thus indicate that interplanetary transport effects influence the pickup ion distributions (Möbius et al. 1996).

At this point, the uncertainties for the temperature determination of He are still rather large because the degree of suppression of the data flow between IBEX-Lo and the CEU is poorly known. This suppression is rate dependent, and the strength of this effect could only be coarsely constrained by available observations. A series of tests with a CEU and IBEX-Lo simulator combination is being carried out to better quantify this effect. In addition, the ISM flow data will be augmented next year with alternating observations in IBEX-Lo high and low angular resolution mode (Fuselier et al. 2009) during the ISM flow peak passages. This operational mode provides simultaneous observations with the full geometric factor and a reduction by a factor of 20, enabling direct determination of the rate dependence of the suppression. The results from these two studies will reduce the uncertainties substantially, including for the observations presented in this paper.

The determination of the combined O + Ne temperature is not affected by the rate-dependent suppression and therefore has already a much smaller uncertainty. As can be seen from the bottom right panel of Figure 8, the combined O + Ne temperature is in agreement with the He temperature and consistent with an isothermal ISM, if we adopt the minimum correction for data loss. However, the O + Ne temperature curve seems to lie slightly higher than that for He. If the He temperature has to be further adjusted downward, the O + Ne temperature (with O being the majority species) would turn out to be higher than that of He, a rather tantalizing result, which could suggest that the species are not in thermal equilibrium with each other. Yet, any further discussion at this point is subject to the remaining uncertainties, which will be reduced in the coming years.

In addition to the planned studies, the *IBEX* orbit has just been modified to a lunar synchronous orbit (McComas et al. 2011a) that remains stable over several decades. As a consequence, the orbit period is slightly longer (≈9.1 days), thus requiring a second adjustment of the spin-axis orientation near apogee of the orbit. For the ISM flow observations, this new operations' strategy will provide observations that overlap at the "Sun-pointing location" near apogee, where aberration of the ISM flow due to spacecraft motion is negligible. Also, the "Sun-pointing location" will overlap with the observation intervals. Therefore, starting next year, we will not need to apply extrapolations to the observations, which will substantially improve the accuracy of the analytical determination of the ISM flow parameters. In addition, we will obtain observations at twice as many different "Sun-pointing locations." Furthermore, the detailed analysis of the star sensor data has provided evidence that the IBEX-Lo pointing coincides exactly with the nominal pointing as obtained from the *IBEX* attitude data and that de-spinning of data sets during star tracker blinding can be performed to $<0.^{\circ}1$ accuracy (Hlond et al. 2012). Therefore, the current data volume will grow by more than a factor of two, and several cases of long extrapolations to the "Sun-pointing location" can be avoided. In combination, this will substantially improve the fidelity of the ISM flow observations and drastically reduce uncertainties.

To conclude the current discussion, we note two further entries in Figure 13. Shown are the velocities of the LIC and the G-Cloud, with their respective error bars, obtained

by Redfield & Linsky (2008) with rather small uncertainties. Previous determinations of the local ISM flow velocity have indicated a value that represents more or less the average for the two clouds. This average value had led to the speculation that our solar system might be in transition between the two clouds. If the values reported here settle around their current center value, after reducing the error bars, we may find ourselves still fully in the LIC. However, such a conclusion should await further refinement of the analysis.

The authors are grateful to the many individuals at the *IBEX* co-investigator institutions who have made this project possible. This work is supported by the Interstellar Boundary Explorer mission as a part of NASA's Explorer Program and partially by NASA SR&T Grant NNX10AC44G, the Swiss National Science Foundation, PRODEX, and the Space Research Centre of the Polish Academy of Sciences. We thank the referee for extremely helpful comments and suggestions.

APPENDIX A

INSTRUMENTAL EFFECTS RELATED TO THE DATA SELECTION

A.1. Data Selection Related to Pointing Issues

As pointed out in Section 2, the analysis of the flow distributions in latitude requires precision knowledge of the IBEX-Lo pointing at any time. However, during time periods when the operation of the *IBEX* star tracker is impaired by intense light sources (such as the Earth and the Moon) in its FoV over a substantial fraction of its spin scan, the spin pulse (which signals that IBEX-Lo points 3° before passing the southern ecliptic pole) is missing. During these times, the pulse height events of the two *IBEX* sensors are time-tagged by the CEU in a free running mode using the last reliable spin period. This value is not precisely correct over long intervals, and, as a result, the *IBEX* coordinate system drifts slowly in spin phase over time. Using the ISM flow or bright stars as observed with the IBEX-Lo star sensor as markers, the coordinate system is de-spun. Small uncertainties in the de-spinning process do not influence the ISM flow count rate that is obtained over $\pm 3\sigma$ of the angular distribution from the peak position in latitude. For the analysis of the angular flow distributions, used in Sections 4 and 5, however, we are currently only selecting time periods, when the star tracker performs within specifications. In addition to some uncertainties about the accuracy of the de-spinning to better than 0.°2, there are reasons to adhere to time periods that do not require post-processing of the spin phase, as discussed below.

A.2. Data Selection Related to CEU Data Transfer Issues

By concentrating on heliospheric ENAs, *IBEX* is a mission with rather low count rates. Therefore, the full information for individual ENAs is transmitted as the highest resolution data. Each such event is time-tagged so that its arrival direction in spin phase can be known with a precision of 0.°04. This data product would be ideal for the ISM flow analysis. However, for magnetospheric ENAs (e.g., Fuselier et al. 2010; McComas et al. 2011b; Petrinec et al. 2011) and the ISM flow, the count rates are so high that they affect onboard data processing. Specifically, the transmission between the IBEX-Lo sensor and the CEU that formats the information for the telemetry slows down owing to both the total traffic across that interface and the computational load on the CEU. This load also includes generating histograms of counts accumulated in 6° angle bins. The transmission speed is modulated by this histogram accumulation scheme.

As anticipated, the number of counts accumulated in the peak of the ISM flow distributions (and magnetospheric emissions) exceeds the telemetry allocation. Thus, in order to avoid filling of the telemetry buffer with high rates of peaked distributions, telemetry slots are allocated within each 6° sector. This scheme leads to a drop in the transmitted event rate toward the end of each 6° sector in the center of the ISM flow peak. However, by design, these events are still accumulated in internal histograms. For the current analysis, we restrict our analysis to 6° data that are readily corrected for these effects in the histograms.

The collimator bias voltages of IBEX-Lo were supposed to provide additional protection against electrons and ions. However, the IBEX-Lo positive collimator voltage could not be brought to operational values, and thus the negative voltage is kept at a low value. As a result, on average IBEX-Lo counts 22 electrons s^{-1}. These electrons do not produce ENA background because the triple coincidence system can easily remove these events that have very short TOFs. However, these electrons contribute to the load on the CEU, which removes them from the event stream. During times when IBEX-Hi observes substantial solar wind related background (Schwadron et al. 2011) the electron rate increases in IBEX-Lo, reducing the throughput of valid ENA events, which in turn results in a noticeable reduction in the ISM flow data. These time periods can easily be identified in the IBEX-Lo TOF rates and in the IBEX-Hi background signals and are also removed from analysis.

APPENDIX B

INSTRUMENTAL EFFECTS ON THE WIDTH OF THE ISM FLOW DISTRIBUTION

The width of the angular flow distributions is substantially affected by the rate-dependent computational load of the CEU and the limited throughput of the IBEX-Lo–CEU interface as described in Section 2.4 and Appendix A. This is particularly true for distributions at the ISM flow maximum. The higher the observed rate, the lower the fraction of particles counted and accumulated by the CEU. Since the count rate varies with the spin phase, the relation between observed rates and throughput is also a function of the spin angle. Therefore, the observed angular distributions appear wider than the original distributions. If uncorrected, this would translate into derivation of an apparently higher temperature. However, the location of the peak in latitude, as well as the longitude of the ISM flow maximum, appears to not be affected significantly as has been tested by comparing de-spun data of the peak orbits with the "good" time data, where the peaks appear to agree within the fitting uncertainties.

In the following, we treat the rate-dependent reduction of the observed rate due to the limitations in the CEU throughput as equivalent to a dead time τ_D of a detector system. Because a digital interface and computational loads are involved, the effects may not be strictly stochastic, but for the 6° angular binning and the time periods used for accumulation, potential non-stochastic effects should be inconsequential. If the equivalent dead time τ_D of a system is known, the observed rates R_{Obs} can be corrected for the reduction to yield the approximate true incoming rate R_{In},

$$R_{In} = \frac{R_{Obs}}{1 - (R_{Obs} + R_{BG})\tau_D}. \quad \text{(B1)}$$

Here, R_{BG} is the total of all additional background rates, such as the rate of electrons that must be separated from the signal

Table 2
Compilation of Symbols Used and Their Definition

Symbol	Definition
$\lambda_{ISM\infty}$	In-ecliptic angle of the interstellar flow at infinity
$\beta_{ISM\infty}$	Latitudinal angle of the interstellar flow at infinity
$V_{ISM\infty}$	Interstellar bulk flow speed relative to the Sun at infinity
$V_{ISM}(1AU)$	Interstellar bulk flow speed at 1 AU
T_{He}, T_{O+Ne}	Temperatures of neutral interstellar gas species; if the subscript is dropped, the temperature can apply to any species
λ_{Obs}	Position of the observer in ecliptic longitude
θ_∞	Angle swept out by the radius vector of the hyperbolic trajectory of an interstellar neutral atom from infinity to the observer at 1 AU, or true anomaly at infinity
V_∞	Speed of any interstellar atom in the velocity distribution at infinity
λ_{Peak}	Position of the peak interstellar gas flow at 1 AU in ecliptic longitude
ψ_{Peak}	Peak of the interstellar gas flow distribution at 1 AU in ecliptic latitude
$M_{ISM\infty}$	Mach number of the interstellar gas flow at infinity
C_∞	Sound speed of the interstellar gas at infinity (can apply to any species)
σ_ψ	Sigma width of the observed interstellar gas flow at 1 AU in ecliptic latitude
σ_λ	Sigma width of the observed interstellar gas flow at 1 AU in ecliptic longitude
χ_∞	Sigma width of the interstellar gas distribution at infinity (deduced from 1 AU observations)
r_E	Distance of the Earth from the Sun
ν_{Ion}	Total ionization rate at 1 AU
R, R_o	Rate of the interstellar flow at 1 AU with (R) and without (R_o) extinction along the trajectories due to ionization
δ	Out-of-ecliptic angle of the *IBEX* spin axis
$T_{He\ UL,\ LL}$	Temperature of interstellar He, derived with estimated minimum (UL) and maximum (LL) rate-dependent data suppression
τ_D	Equivalent dead time in the event processing through the CEU
R_{Obs}, R_{In}, R_{BG}	Observed (Obs), incoming (In), and background rate (BG) relevant for the evaluation of rate-dependent suppression in the data throughput of the CEU

by the CEU (typically 22 counts s^{-1}). The IBEX-Lo interface hardware has been designed and tested to yield an equivalent dead time $\tau_D = 1.2$ ms, which sets a minimum dead time to be considered here. The CEU is likely to increase this value noticeably. In order to estimate the overall equivalent dead time of the system, we compared the angular width of the spin angle distributions during the orbits close to the ISM flow peak in 2009 and 2010 for energy steps 2 and 4. Step 2 is used throughout the analysis because of its high sputtering yield and its flat response to the incoming particle energy. In energy step 4 the rate is lower by a factor of ∼5 because it is close to the ISM flow bulk energy at 1 AU (as can be seen schematically from Figure 1). This step is good for comparisons because the lower particle rate reduces the CEU load. Based on a comparison of the widths of the distributions, a dead time of up to 5 ms was derived. This estimation is not very accurate because various assumptions had to be made. Therefore, we include a large range of 1.2–5 ms for the equivalent dead time in our present analysis, which translates into a substantial uncertainty for the width of angular distributions and thus the temperature. However, the other parameters under evaluation are not affected by this correction and thus have significantly smaller uncertainties.

APPENDIX C

USE OF SYMBOLS IN THE PAPER AND THEIR DEFINITION

Throughout this paper, unprimed symbols (e.g., ψ_{Peak}) refer to quantities in the rest frame and primed symbols (e.g., ψ'_{Peak}) in the observer frame, i.e., moving with the Earth. Angles in ecliptic longitude (λ) are referenced to the Sun's position in the sky at spring equinox. Table 2 gives a compilation of all symbols used and the definitions, except those that are commonly used in scientific notation.

REFERENCES

Alexashov, D., & Izmodenov, V. 2005, A&A, 439, 1171
Axford, W. 1972, in Solar Wind, ed. E. P. Sonnett, P. J. Coleman, & J. M. Wilcox (NASA SP-308; Washington, DC: Scientific and Technical Information Office, NASA), 609
Banaszkiewicz, M., Witte, M., & Rosenbauer, H. 1996, A&AS, 120, 587
Bertaux, J., & Blamont, J. 1971, A&A, 11, 200
Bochsler, P., Petersen, L., Möbius, E., et al. 2012, ApJS, 198, 13
Bzowski, M., Kubiak, M., Möbius, E., et al. 2012, ApJS, 198, 12
Cheng, K., & Bruhweiler, F. 1990, ApJ, 364, 573
Cox, D., & Reynolds, R. 1987, ARA&A, 25, 303
Crutcher, R. 1982, ApJ, 254, 82
Fahr, H. 1974, Space Sci. Rev., 15, 483
Fahr, H., Kausch, T., & Scherer, H. 2000, A&A, 357, 268
Frisch, P. C. 1981, Nature, 293, 377
Frisch, P. C. 1995, Space Sci. Rev., 72, 499
Frisch, P. C. 2006, Solar Journey: The Significance of Our Galactic Environment for the Heliosphere and Earth, Vol. 338 (Dordrecht: Springer)
Frisch, P. C., Bzowski, M., Grün, E., et al. 2009, Space Sci. Rev., 146, 235
Funsten, H. O., Allegrini, F., Bochsler, P., et al. 2009, Space Sci. Rev., 146, 75
Fuselier, S., Bochsler, P., Chornay, D., et al. 2009, Space Sci. Rev., 146, 117
Fuselier, S., Funsten, H., Heirtzler, D., et al. 2010, Geophys. Res. Lett., 37, L13101
Gloeckler, G., & Geiss, J. 1998, Space Sci. Rev., 86, 127
Gloeckler, G., & Geiss, J. 2001, in AIP Conf. Proc. 598, Solar and Galactic Composition: A Joint SOHO-ACE Workshop, ed. R. F. Wimmer-Schweingruber (Meville, NY: AIP), 281
Gloeckler, G., Geiss, J., Balsiger, H., et al. 1992, A&A, 92, 267
Gloeckler, G., Möbius, E., Bzowski, M., et al. 2004, A&A, 426, 897
Hlond, M., Bzowski, M., Möbius, E., et al. 2012, ApJS, 198, 9
Holzer, T. 1977, Rev. Geophys. Space Phys., 15, 467
Jokipii, J. 1998, Space Sci. Rev., 86, 161
Klecker, B. 1995, Space Sci. Rev., 72, 419
Lallement, R., & Bertin, P. 1992, A&A, 266, 479
Lallement, R., Möbius, E., Bzowski, M., et al. 2004, A&A, 426, 897
Lee, M., Kucharek, H., Möbius, E., Wu, X., Bzowski, M., & McComas, D. 2012, ApJS, 198, 10
Linsky, J., Brown, A., & Gayley, K. 1993, ApJ, 402, 694
McClintock, W., Henry, R., Linsky, J., & Moos, W. 1978, ApJ, 225, 465
McComas, D. J., Allegrini, F., Bochsler, P., et al. 2009a, Space Sci. Rev., 146, 11
McComas, D. J., Allegrini, F., Bochsler, P., et al. 2009b, Science, 326, 959
McComas, D. J., Carrico, J. P., Hautamaki, B., et al. 2011a, Space Weather, 9, S11002
McComas, D. J., Dayeh, M. A., Funsten, H. O., et al. 2011b, J. Geopys. Res., 116, A02211
McComas, D. J., Ebert, R., Elliott, H., et al. 2008, Geophys. Res. Lett., 35, L18103
McComas, D. J., Schwadron, N. A., Crary, F. J., et al. 2004, J. Geophys. Res., 109, A02104
McMullin, D. R., Bzowski, M., Möbius, E., et al. 2004, A&A, 426, 885
Möbius, E. 2009, Space Sci. Rev., 143, 465
Möbius, E., Bochsler, P., Bzowski, M., et al. 2009a, Science, 326, 969
Möbius, E., Bzowski, M., Chalov, S., et al. 2004, A&A, 426, 897
Möbius, E., Bzowski, M., Müller, H., & Wurz, P. 2006, in Solar Journey: The Significance of Our Galactic Environment for the Heliosphere and Earth, ed. P. C. Frisch (Dordrecht: Springer), 206
Möbius, E., Hovestadt, D., & Klecker, B. 1985, Nature, 318, 426
Möbius, E., Klecker, B., Bochsler, P., et al. 2010, in AIP Conf. Proc. 1302, Pickup Ions throughout the Heliosphere and Beyond, ed. J. le Roux, G. P. Zank, A. J. Coates, & V. Florinski (Melville, NY: AIP), 37

Möbius, E., Kucharek, H., Clark, G., et al. 2009b, Space Sci. Rev., 146, 149
Möbius, E., Rucinski, D., Isenberg, P., & Lee, M. 1996, Ann. Geophys., 14, 492
Müller, H., Florinski, V., Heerikhuisen, J., et al. 2008, A&A, 491, 43
Müller, H., & Zank, G. 2004, J. Geophys. Res., 109, A07104
Petrinec, S., Dayeh, M., Funsten, H. P., et al. 2011, J. Geophys. Res., 116, A7
Redfield, S. 2008, Space Sci. Rev., 143, 323
Redfield, S., & Linsky, J. 2008, ApJ, 673, 283
Richardson, J., Paularena, K., Lazarus, A., & Belcher, J. 1995, Geophys. Res. Lett., 22, 1469
Saul, L., Wurz, P., Möbius, E., et al. 2012, ApJS, 198, 14
Schwadron, N. A., Allegrini, F., Bzowski, M., et al. 2011, ApJ, 731, 56
Slavin, J., & Frisch, P. 2002, ApJ, 565, 364
Smirnov, B. 1982, Negative Ions (New York: McGraw-Hill)
Tarnopolski, S., & Bzowski, M. 2008, A&A, 483, L35
Vallerga, J., Lallement, R., Raymond, J., et al. 2004, A&A, 426, 855
Weller, C., & Meier, R. 1974, ApJ, 193, 471
Witte, M. 2004, A&A, 426, 835
Witte, M., Banaszkiewicz, M., & Rosenbauer, M. 1996, Space Sci. Rev., 78, 289
Wolff, B., Koester, D., & Lallement, R. 1999, A&A, 346, 969
Wurz, P., Saul, L., Scheer, J., et al. 2008, J. Appl. Phys., 103, 054904
Zank, G. P., & Müller, H. R. 2003, J. Geophys. Res., 108, 1240
Zank, G. P., Müller, H., Florinski, V., & Frisch, P. 2006, in Solar Journey: The Significance of Our Galactic Environment for the Heliosphere and Earth, ed. P. C. Frisch (Dordrecht: Springer), 23
Zank, G., Pogorelov, N., Heerikhuisen, J., et al. 2009, Space Sci. Rev., 146, 295